Coupling nitrogen vacancy centre spins in nanodiamonds to external fields

By

Sarath Raman Nair

A thesis submitted to Macquarie University

for the degree of Master of Research

Department of Physics

June 2016

MACQUARIE
University
SYDNEY·AUSTRALIA

Typeset in LaTeX 2_ε.

Except where acknowledged in the customary manner, the material presented in this thesis is, to the best of my knowledge, original and has not been submitted in whole or part for a degree in any university.

Sarath Raman Nair

Acknowledgements

I would like to thank my supervisor Dr Thomas Volz for his guidance and intellectual support over the past year.

I would also like to thank Dr Carlo Bradac, A/Prof Gavin Brennen, Dr Xavier Vidal, Dr Sukhwinder Singh and PhD candidates Matthew Van Breugel, Andrew Wood, Thomas Guff for their role in mentoring and supporting me during my Master Project.

Finally, I would like to thank my love Jemy and my family for their encouragement and support over my many years of study.

Abstract

This thesis focuses on the spin physics of nitrogen-vacancy (NV) centres in nanodiamonds (NDs) via their coupling to external fields. In the first part, we theoretically investigate the feasibility of coupling a ND with a high density of NV centres to a gap-tunable flux qubit. We calculate the optimum position including the tolerance for maximizing the coupling and calculate its dependence on the orientation of the ND. We demonstrate that the coherent coupling of a 150-nm ND containing many (10^3) NV centres and a flux qubit with dephasing time of $\sim$1 μs is feasible. In the second part, we investigate the spin-coherence properties of NV centres in NDs and discuss them in the context of the NVs-to-flux qubit coupling. In particular, we manipulate the NV spins via an external microwave field using two distinct methods. The first, more conventional method employs a thin wire in direct contact with the sample as the microwave antenna. The second method has been developed by our group. It uses a cavity to produce the microwave field at the position of the NV spins with the advantage over the wire architecture of addressing the NV centre spins, without sample heating and over macroscopic spatial distances (milli-meters versus micro-meters).

Contents

List of Figures

It doesn't matter how beautiful your theory is, it doesn't matter how smart you are. If it doesn't agree with experiment, it's wrong.

Richard P. Feynman

1

Introduction

Today, colour centres in diamond have been accredited as prominent candidates for cutting edge quantum (nano) technologies. Pure diamond is transparent due to its wide 5.5 eV band gap at room temperature [1, 2]. However, diamond is host to lattice defects with specific optical transitions lying in the diamond band gap between the ground and excited states. Such defects are therefore responsible for the different colours of diamond and are, hence, often referred to as 'colour centres'. Diamond is host to more than five hundred colour centres [3, 4]. Out of them, the nitrogen-vacancy (NV) colour centre in its negative charge state is probably the most studied one in diamond as it posses unique optical and spin properties at room temperature. It is the only known solid-state quantum system that works at ambient conditions and it finds applications ranging from quantum information technologies to high-resolution sensing and biomedicine [1].

1.1 Background and motivation

Qubit systems that can coherently process quantum information and store it for the desired amount of time is one of the primary drives in quantum technology research. The NV^- centre is an interesting quantum system, which is considered amongst the most suitable qubits. The speciality of the NV^- is its weak interaction with the environment, which leads to outstanding coherence time properties. It is the only known solid-state qubit system that works at room-temperature [5]. The coherence time of the electronic spin in the NV^- can reach up to ~2 ms at room temperature [6], which is remarkable. Apart from that, unlike other atomic systems such as trapped ions or ultra-cold atoms, the NV^- centre in diamond, being a solid state system, is comparatively easy to handle and prepare. On the other hand, due to the relatively weak interaction with external fields, the processing speed of the NV^- centre is not up to the mark. One way to circumvent the problem is to couple the NV^- centre to other qubit systems which possess complementary properties. The most interesting qubit systems that possess the desired complementary properties are macroscopic superconducting (SC) systems like flux qubits [7, 8]. In this context, the scope of my thesis is twofold: first to look into coupling NV^- centres in nanodiamonds to flux qubits by numerical calculations and the second is to characterize and study the coherence properties of NV^- centres specifically in nanodiamonds.

In 2010, D. Marcos, et al. [7], and simultaneously J. Twamley and S. D. Barret [9] proposed the idea of coupling NV^- centres to a SC flux qubit. They chose the NV^- centre over other systems due to its unique quantum properties even at ambient conditions. Followed by their proposal, experimental studies of coupling ensembles of NV^- centres in bulk diamonds to gap tunable flux qubits have been reported [10–13]. For coherent coupling, these experiments used about $\sim 10^7$ spins in bulk diamond. However, the coherent coupling regime can also be reached with less spins if the NV^- centres are positioned very close to the flux qubit. In bulk diamond this is almost impossible and it is the reason why we propose an alternative approach. We consider a small nanodiamond (~150 nm) containing many ($\sim 10^3$) NV^- centres in nanodiamonds. It can be precisely placed on the flux qubit, so that coherent coupling can be achieved with few thousand spins or even less. The challenge is to improve considerably the coherence times of both systems, so that the coupling will last for the desired amount of time. This motivates the present study of investigating the coherent coupling of NV^- centres

in nanodiamonds to the flux qubits, as a new direction we are pursuing. In the first part of my thesis, I carry out a numerical simulation, discussing the feasibility of our proposal.

In the second part of my thesis I then proceed with describing an experimental study of the coherence properties of single NV^- centres in nanodiamonds in order to explore if they are consistent with the requirements established from the numerical calculations of NV^--flux qubit coupling strengths. In order to do this we use a well established pulse optically detected magnetic resonance (ODMR) technique involving laser fields and microwave (MW) fields. Our research group previously developed a dielectric micro-wave cavity [14] in collaboration with Prof M. E. Tobar's research group at The University of Western Australia (UWA). This microwave cavity can address the NV^- spins on a milli-metre scale, without much sample heating or sample drift which is a problem with conventional wire based methods. While the group has previously demonstrated continuous ODMR measurements [14], this thesis reports on the first successful pulsed ODMR measurement with this cavity. From a more general perspective, the experiments described here establish for the first time coherent spin manipulation as a tool in the Diamond Nanoscience Lab at Macquarie University.

1.2 Outline of the thesis

Chapter 2 briefly reviews the basic properties of the NV^- centre relevant for this thesis.

Chapter 3 presents the numerical study of coupling NV^- centres in nanodiamonds to a gap-tunable flux qubit. Our results show that in principle it is possible to achieve coherent coupling with only a few thousand spins. We calculate the coupling strength dependence on the precise positioning of the nanodiamond on the flux qubit, and on the orientation of the NV^- centre quantization axis. The latter is important due to the random orientation of the nanodiamond crystal when placed on the flux qubit.

Chapter 4 explains the experimental methods and the experimental setup we employ for coherent spin manipulation and the characterization of spin-coherence times for single NV^- centre coupled to a MW field. Particular emphasis is put onto explaining the MW cavity.

Chapter 5 presents the results of our spin manipulation experiments and spin echo-studies for single NV^- centres by coupling them to external MW fields by both using the standard technique of micro-wire and our original method of the MW cavity.

Chapter 6 closes this thesis and presents important conclusions based on the numerical and experimental results presented in the previous chapters.

2

Nitrogen-Vacancy colour centres in diamond

The nitrogen-vacancy (NV) centre in diamond is a solid-state quantum emitter which possesses unique spin and optical properties at room temperature. This chapter is a short review about the physics of the diamond NV centre, more precisely of the negatively charged NV^- centre, which helps to understand the studies presented in this thesis. The chapter begins with an introduction to the structure of the NV centre with an emphasis on NV^- in section 2.1, and then proceeds to the centre spin properties. The research presented in the thesis focuses exclusively on the electronic spin physics of the NV^- centre. This chapter thus gives a short overview about its spin features (section 2.2), optical spin polarization and coherent spin manipulation (section 2.3), and a short discussion of relaxation times that affect the dynamics of the electronic spin (section 2.4).

2.1 NV colour centre

Diamond is a unique material which possesses several extreme properties including hardness, high thermal conductivity, electron affinity etc. It is composed of carbon atoms having sp^3 hybridised bonds. The NV colour centre (shown in figure 2.1a) is an extrinsic point defect. It forms inside the diamond lattice where it replaces one carbon atom with a substitutional nitrogen atom and another adjacent one with a vacancy, oriented along one of the four crystallographic [111] directions and displaying C_{3v} triagonal symmetry [1, 15]. Being a group five element, the substitutional nitrogen atom has five valence electrons and thus forms three covalent bonds with three neighbouring carbon atoms and one dangling bond with the vacancy. The three carbon atoms neighbouring the vacancy form each a dangling bond and share an electron with it.

The NV centre exists in two charge states, the neutral charge state, known as NV^0, which is a spin-1/2 system and the negative charge state, known as NV^-, which is a spin-1 system. In the NV^0 state, five electrons interact with the vacancy; two from the Nitrogen atom and three from three carbon atoms forming dangling bonds with the vacancy, giving the NV^0 a spin-1/2 character. However, if an electron from somewhere else in the diamond lattice, usually from another impurity nitrogen atom, also called P1 centre [16], is captured by the vacancy, then the NV centre is negatively charged, known as NV^-. At the same time, it turns into a spin-1 system as a total of six electrons are involved with the vacancy. Experimentally, the simplest distinguishing factor between NV^0 and NV^- is the spectral position of the zero phonon line (ZPL) (figure 2.1b). The NV^0 has its ZPL at 575 nm whereas the NV^- at 637 nm [15, 17, 18].

The present thesis concentrates on the NV^- centre, since its spin displays unique optically induced polarisation (or initialization), optical readout and outstanding coherence properties [15, 19]. Therefore, from here on, the NV^- centre will simply be denoted as 'NV' centre without '$^-$' for brevity.

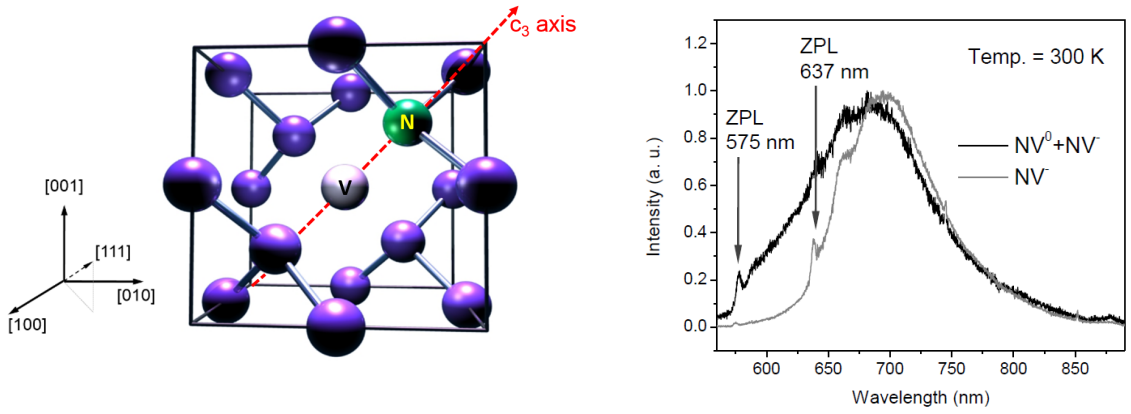

(a) (b)

Figure 2.1: (**a**) NV centre inside the diamond lattice with quantization axis (NV axis or the C_3 axis mentioned in the figure) along one of the [111] direction. Here the nitrogen atom, vacancy, and carbon atoms are shown in green, white and purple, respectively, and the sp^3 bonds are represented by 'sticks'. (**b**) Room temperature (300 K) photo-luminescence (PL) spectra with both charge states of the NV centre present (black line) and with only NV^- (grey line). The spectrum shows the ZPLs of both charge states along with their vibronic side bands [1].

2.2 Electronic spin of the NV centre

As pointed out in section 2.1, the NV centre is a spin-1 system which consists of six electrons. While it is often referred to as a 'single atom' inside the diamond matrix, the spin properties of the NV centre indicate a more complex nature. In this regard, an overview on the electronic spin of the NV centre is necessary in the interest of this thesis.

2.2.1 NV centre excitation

The NV is a colour centre which emits photons as a result of the optical transition between its ground and excited electronic states, which are triplet states. The excitation process is better captured by considering molecular orbits (MOs), rather than atomic orbitals (AOs).

There are four atomic orbitals involved in the NV centre; one from the nitrogen and three from the carbon atoms which form dangling bonds with the vacancy. The linear combination of atomic orbitals leads to the construction of four molecular orbitals (MOs). A further mixing of two of the newly constructed MOs takes place, due to the Coulomb interaction between the electrons, which gives four resultant MOs denoted as $a1'$, $a1$, e_x and e_y [21, 22]. The $a1'$ is located in the valence band and the three MOs $a1$, e_x, and e_y are in between

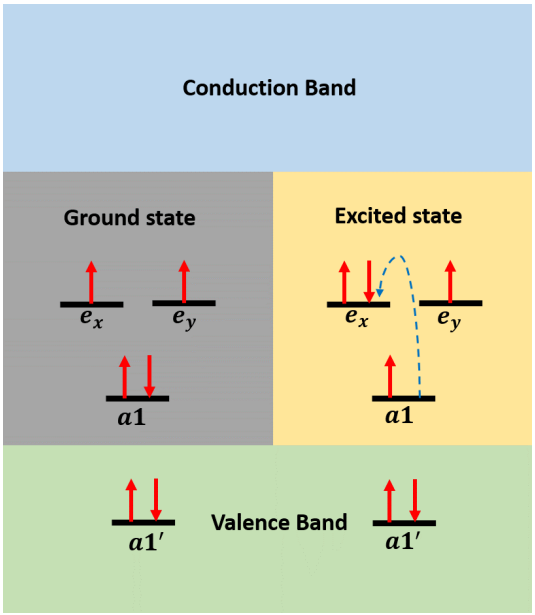

Figure 2.2: Electronic configurations of ground and excited triplet states of the NV centre, based on the concept of MOs. The NV centre excitation is shown as the excitation of an electron indicated by the curved blue dashed arrow. Image adapted from [20].

the diamond valence and conduction bands (figure 2.2) [21, 22]. The MOs are arranged in terms of energy based on the symmetry and Coulomb interactions and following Hund's rule, the six electrons involved in the NV centre get filled in the MOs as shown in figure 2.2 [22]. The $a1'$ level is not involved in the excitation of the centre, whereas the other three resultant MOs are corresponding to the excitation of an electron from $a1$ to either e_x or e_y (denoted by the blue dashed curve in figure 2.2). One important thing to note is that both the nitrogen and carbon atomic orbitals are contributing significantly to $a1$, whereas e_x and e_y have contributions only from carbon orbitals [21]. Note that in both the excited and ground states there are two unpaired electrons and the interaction between them results in a splitting in both the ground and excited spin triplet states at zero magnetic field [20].

2.2.2 Electronic spin energy level scheme

The ground and excited triplet states, along with two experimentally detectable singlet states located in between the excited and ground states [23, 24], are usually described with a simplified spin energy level scheme (figure 2.3) [15], which captures the core physics of the NV centre.

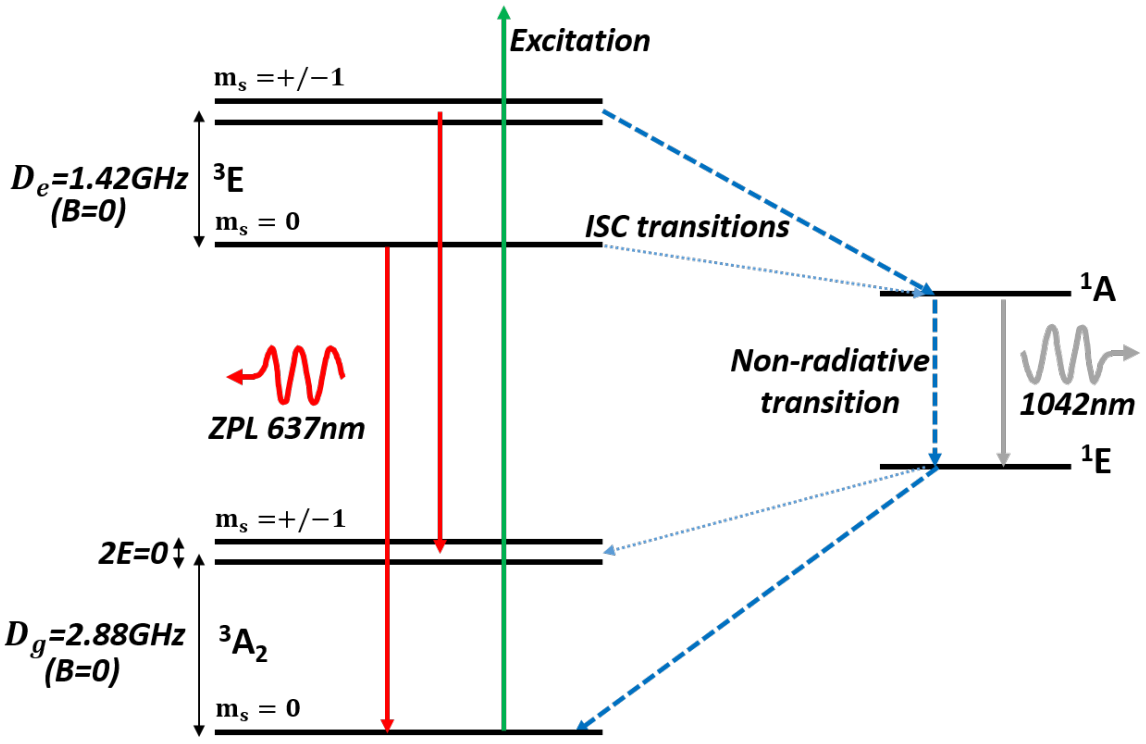

Figure 2.3: Simplified spin energy level scheme of the NV centre in the absence of any strain or magnetic fields. The green arrow represents the (off-resonant) excitation of the NV centre from the ground triplet state ($^3A_2$) to the excited triplet state (^{3}E), while radiative transition between them gives the characteristic ZPL of 637 nm. Significant and negligible inter-system crossing (ISC) transitions from ^{3}E to ^{1}A and ^{1}E to $^3A_2$ are shown in blue dashed and dotted arrows, respectively. The radiative transition between ^{1}A and ^{1}E corresponds to emission of light at 1042 nm [23, 24].

The triplet ground and excited states are denoted as $^3A_2$ and ^{3}E, respectively, while the two intermediate singlet states are denoted as ^{1}A and ^{1}E. The triplet states are given in terms of m_s, which is the projection of the spin along the quantization axis of the NV [19, 25, 26]. The excited state ^{3}E has a zero field splitting $D_e \sim 1.42$ GHz between the $m_s = 0$ and $m_s = \pm 1$ states, along the quantization axis; in the absence of any stress, the $m_s = +1$ and $m_s = -1$ states are degenerate [27, 28]. The excited triplet state ^{3}E has a lifetime of ~12 ns for the $m_s = 0$ and ~7.8 ns for $m_s = \pm 1$ states [29]. Of the two singlet states, the upper one ^{1}A has a lifetime $\lesssim 1$ ns and the lower one ^{1}E, of 219 ns at room temperature (295K) [24].

The ground triplet spin state ($^3A_2$) of the NV centre needs to be explained in more detail as it is important for this thesis. The following section 2.2.3 explores it.

2.2.3 Ground state of the NV centre

The ground triplet spin state can be explained with a ground-state spin Hamiltonian. Neglecting any hyperfine interactions between the electronic spin and the nearby nuclear spin (as we are concentrated only on the electronic spin of the NV) and by choosing the quantization axis of the NV as the z-axis, the ground-state Hamiltonian can be written as [19],

$$H_{gs} = \hbar D_g S_z^2 + \hbar E(S_x^2 - S_y^2) + g_e \mu_B \mathbf{B} \cdot \mathbf{S}, \tag{2.1}$$

where, $\hbar$ is the reduced Planck's constant ($h/2\pi$), $D_g/2\pi \sim 2.88$ GHz is the zero field splitting which arises due to the interaction between the spins of the two unpaired electrons in the MOs e_x and e_y, E is the strain-induced splitting between the $m_s = \pm 1$ levels of the ground triplet states, g_e is the electron g-factor, μ_B is the Bohr magneton, B is the external magnetic field potentially acting on the NV and $\mathbf{S}(S_x, S_y, S_z)$ are the Pauli matrices for the spin-1 operators.

The last term of the equation 2.1 is the Zeeman interaction term and can be expanded in x-, y- and z-coordinates. However, restricting ourself to the weak magnetic field regime that does not affect the quantization axis, we can neglect the x and y components of the Zeeman interaction term [19]. Then the ground state spin Hamiltonian can be rewritten in matrix form as,

$$H_{gs} = \begin{bmatrix} \hbar D_g + g_e \mu_B B_z & 0 & \hbar E \\ 0 & 0 & 0 \\ \hbar E & 0 & \hbar D_g - g_e \mu_B B_z \end{bmatrix} \tag{2.2}$$

The diagonalization of the ground state spin Hamiltonian matrix in equation 2.2 gives the ground state energy splitting between $m_s = \pm 1$ and $m_s = 0$ as,

$$\Delta_{\pm} = \hbar D_g \pm \sqrt{\hbar^2 E^2 + (g_e \mu_B B_z)^2} \tag{2.3}$$

Thus the splitting between the $m_s = +1$ and $m_s = -1$ due to the off-axis strain is $2E$ and in the absence of an external magnetic field or in the absence of any stress, $m_s = +1$ and $m_s = -1$ are degenerate. However, we can see from equation 2.3 that in the presence of an external magnetic field along the quantization axis, the degeneracy of $m_s = \pm 1$ will get lifted even in the absence of any stress due to the Zeeman splitting. Figure 2.4 shows the Zeeman splitting of ground state $m_s = \pm 1$ spin states, for the applied magnetic field along

the quantization axis, z.

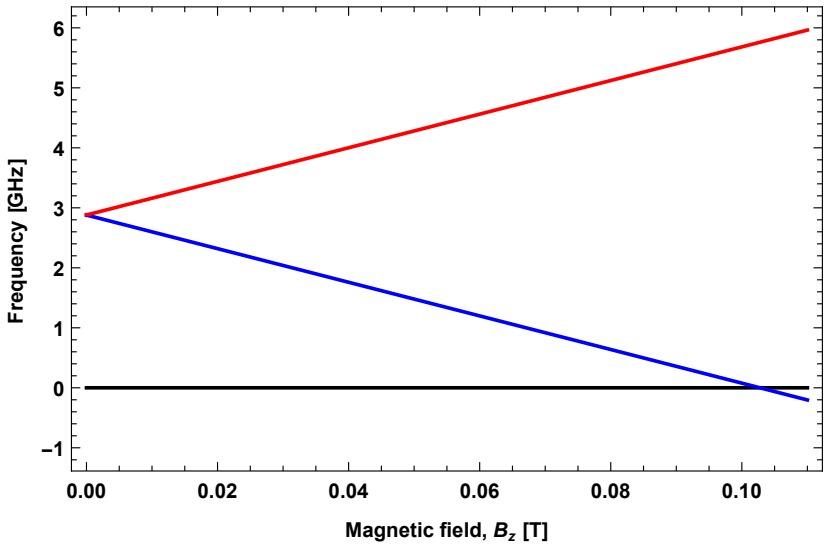

Figure 2.4: Zeeman splitting of ground state $m_s = \pm 1$ spin states with an increasing magnetic field applied along the quantization (z-) axis of the NV centre. The black line represents the $m_s = 0$ state, the blue line represents the $m_s = -1$ state and the red line represents the $m_s = +1$ state. The stress splitting has been taken as $E/2\pi = 5$ MHz [19].

Figure 2.4 has been obtained from equation 2.3, by considering the positions of the $m_s = \pm 1$ spin states relative to the $m_s = 0$ state. The stress induced splitting value is taken as $E/2\pi$=5 MHz, which is a typical value for nanodiamonds [19]. The plot clearly shows that when $B_z \approx 0.1$ T, then the $m_s = 0$ and $m_s = -1$ states would be degenerate in energy, which is referred to as 'level anticrossing' [1]. The Zeeman splitting of the $m_s = \pm 1$ ground spin states can be used to detect an external magnetic field by quantifying the energy splitting, using an experimental method called optically detected magnetic resonance (ODMR). This will be discussed later in chapter 4. The Zeeman splitting in combination with ODMR forms the basis for high resolution magnetometry with NV centres. However, NV based magnetometry is beyond the scope of this thesis and will not be analysed in detail; the interested reader can find more information in a recent review paper [19].

2.3 Manipulation of the NV centre spin

The important feature that enables the use of NV centres for solid state quantum technologies is the external control of the NV centre spin by optical and microwave (MW) fields. The NV centre spin can be initialized into the $m_s = 0$ ground state via optical excitation, while

the coherent manipulation of the spin is usually done by an external MW field resonant with the spin-splitting transition. Recently, the full control of the single NV centre has also been demonstrated via purely optical means at low temperature [30].

2.3.1 Spin polarization of the NV centre

For a given diamond crystal with an ensemble of NVs, the centres are randomly distributed in the spin triplet ground state and the population on each spin state is determined by the Boltzmann steady state distribution. With an excitation of suitable wavelength (for example 532 nm) the NV centres undergo spin selective optical transition ($\Delta m_s = 0$), from $^3A_2$ to ^3E (figure 2.3). Specifically, the NV centres in the $m_s = 0$ and $m_s = \pm 1$ of the $^3A_2$ triplet spin states are excited to the corresponding $m_s = 0$ and $m_s = \pm 1$ of the ^3E triplet spin state. The ^3E triplet state is coupled to the upper singlet state ^1A and the lower singlet state ^1E is coupled to $^3A_2$ through spin-orbit interaction [24]. The NV centres that reach the $m_s = 0$ state of ^3E undergo radiative transition to $m_s = 0$ of $^3A_2$ with emission of photons at 637 nm, while the inter-system crossing (ISC) transitions from $m_s = 0$ of the triplet ^3E state to ^1A are negligible [29]. On the other hand, a considerable portion of NV centres that reach the $m_s = \pm 1$ state of ^3E undergo non-radiative ISC transitions to the ^1A singlet state and undergo a decay along with a radiative transition at 1042 nm between the two singlet states ^1A and ^1E [23, 24]. They ultimately end up in the $m_s = 0$ state of $^3A_2$ from ^1E through the ISC transition; the transitions from ^1E to $m_s = \pm 1$ of $^3A_2$ are instead negligible. This process continues as the excitation persists and after a few optical cycles all the NV centres are polarised to the $m_s = 0$ of the ground triplet state. The spin-polarised NV ensemble does not obey the Boltzmann distribution any more. This is the beauty of the NV centre: the possibility to achieve spin polarization without lowering the temperature below ambient conditions, but just by pumping it optically.

An NV centre polarised into its $m_s = 0$ state of the ground triplet $^3A_2$ displays maximum fluorescence upon excitation as there is no ISC transitions. However, if a MW field in resonance with the energy difference ($\sim$2.88 GHz) of $m_s = 0$ and $m_s = \pm 1$ states of the $^3A_2$ manifold is applied, a decrease in fluorescence intensity is observed as the spin state $m_s = \pm 1$ scatters less photons than the 'bright' $m_s = 0$ state (note that in the ideal case, i.e. no stress or zero magnetic field, $m_s = +1$ and $m_s = -1$ are degenerate. The degeneracy can be lifted

by means of an external magnetic field or induced stress). This property can be used for read out of the NV centre spin.

2.3.2 Spin manipulation of the NV centre in the ground state

The coherent manipulation of the spin polarised NV centre is required for quantum technological applications. This can be achieved with an external MW field. The dynamics of the spin state of spin polarised NV centres can be traced via their fluorescence. By applying a MW frequency resonant with the $m_s = 0$ and $m_s = \pm 1$; the fluorescence reveals an oscillatory behaviour. This oscillation is known as Rabi oscillation between the population of $m_s = 0$ and $m_s = \pm 1$ states of $^3A_2$, with the characteristic frequency known as Rabi frequency. The Rabi oscillation can be understood by visualizing the spin states in the Bloch sphere as shown in figure 2.5.

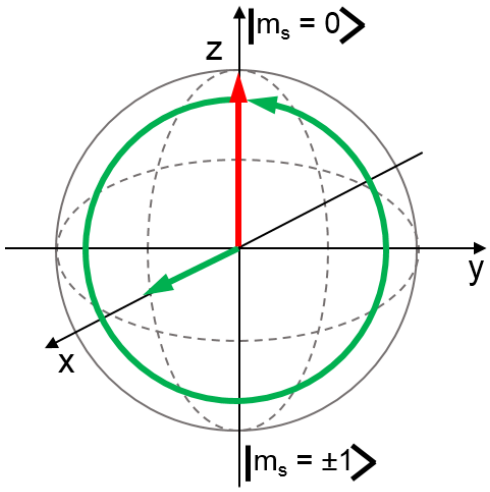

Figure 2.5: Bloch sphere representation of the Rabi oscillation. The red arrow represents the spin state of the NV centre, the green arrow along the x axis represents the externally applied MW field and the green rounded arrow represents the Larmor precession of the spin state around the applied MW field.

The general representation of the spin state in the Bloch sphere is,

$$\left|\Psi_{sp}\right\rangle = \cos\frac{\theta}{2}\left|0\right\rangle + e^{i\phi_{ph}}\sin\frac{\theta}{2}\left|1\right\rangle \tag{2.4}$$

The angle θ is the angle to the state from the z-axis and the phase angle ϕ_{ph} is the angle

to the projection of the state in the x-y plane from the x-axis. Here, we consider the spin polarised system so that the spin state of the syatem in the Bloch sphere is represented along the z-axis (red arrow).

When a resonant microwave field (magnetic field strength H) is applied to the spin polarised system of the NV centre, along the x-axis ($\phi = 0$), the spin will undergo a Larmor precession around the applied field. Then we can represent θ=$\Omega_r t$, where $\Omega_r = \gamma_g H$ is the frequency of the precession known as Rabi frequency, t is the time and γ_g is the gyromagnetic ratio. Thus the spin state oscillates between $|0\rangle$ and $|1\rangle$. [20, 31].

The fluorescence of the NV centre is proportional to the probability of finding the system in $|0\rangle$. The length of the MW pulse for which the spin state of the spin-polarised NV centre inverts from $m_s = 0$ to $m_s = \pm 1$ (correspondingly lower fluorescence) is known as a π pulse ($\theta = \pi$ in the Bloch sphere). For the single NV centre case the measurements have to be repeated many times and integrated over time in order to observe the Rabi oscillation, as for each single event, the optical read-out always projects one of the states [32, 33]. Figure (2.6) shows the oscillation for a single NV centre from our lab, where the number of experimental cycles was 10^6 and the π pulse is on the order of 100 ns.

The Rabi oscillation of a single NV centre shown in figure (2.6) shows an exponentially decaying behaviour. This is due to decoherence, which is basically the irreversible loss of coherence due to interaction with the environment. The dynamics of the spin system determined by different relaxation times, which will be discussed in the next section.

2.4 Relaxation times

The spin polarised NV centre system cannot be coherently manipulated and kept in a superposition state indefinitely as the interaction with the environment adversely affects the system. Where actually, if left alive, an initial coherent state will tend back to a thermally distributed state with no spin coherence. The relaxation time of the system is usually described by means of two different scales corresponding to the so called 'longitudinal electron-spin relaxation time (T_1)' and 'transverse spin phase coherence time (T_2)'.

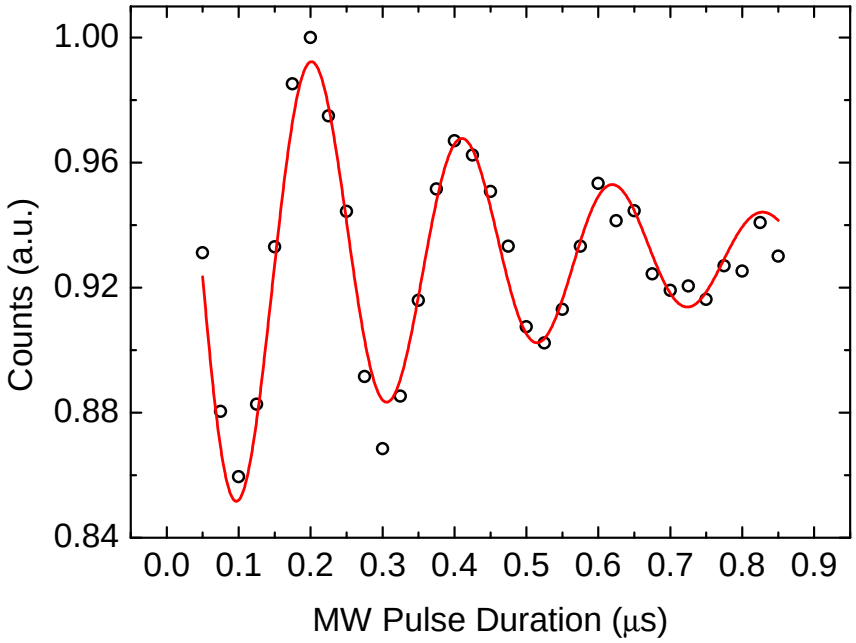

Figure 2.6: Rabi oscilation for a single NV centre, with a π pulse is on the order of 100 ns duration (Ω_r ~4.8 MHz). The solid curve (red) represents a fit to the experimental data points.

T_1 is the lifetime of a spin polarised state and determined by so-called 'longitudinal relaxation' mechanisms which also set the ultimate limit for the phase coherence time. Such relaxation is caused by stochastic processes (e.g. interactions with phonons) which produce irreversible changes in the axial spin projection of the state. In the case of the diamond NV centre, T_1 for the ground-state spin polarization is measured optically thanks to the difference in fluorescence intensities between the spin states $m_s = 0$ ('brighter') and $m_s = \pm 1$ ('darker') [34]. The NV is polarized into the $m_s = 0$ state by means of a 532-nm laser pulse (section 2.3.1) and the centre's fluorescence is read out, after an interval τ of variable length, upon excitation with a second laser pulse. This is done both with and without a MW π-pulse applied right after the polarization pulse. The fluorescence intensities are measured in both cases; their difference is proportional to the residual polarization, after time τ, of only those NVs which were excited by the microwave π-pulse driving the system into the $m_s = \pm 1$ state. By varying the delay τ the dynamic of the longitudinal exponential relaxation T_1 is determined: at room temperature, T_1 for diamond NV centres is in the millisecond range.

T_2 is the measure of time in which loss of phase coherence of spin state is taking place [20] and determined by the (off-resonant) interaction between a single spin and the 'spin bath' of the surrounding environment. This interaction results in the loss of phase memory of the single spin via the dipolar interaction with the fluctuating local field generated by the local spin bath [35]. However, for an ensemble of spins, the local fields vary for each single spin and also, for ensemble measurements of a single spin, the experimental conditions vary for each single measurements [15]. In both cases, the experiments give an average value of the inhomogeneous dephasing times, which is usually denoted as $T_2^* (\leq T_2)$. In the case of the NV centre, the effect of dephasing is visible for instance during a Rabi nutation experiment which probes the $m_s = 0 \leftrightarrow \pm 1$ ground-state spin transition via a resonant microwave field at ~2.88 GHz (section 2.3.2). As demonstrated in figure 2.6, the Rabi oscillation show a decay in its contrast as a function of MW pulse length. The decay is related but not equivalent to T_2, the measurement of which requires a Hahn echo sequence to remove the influences of MW field and the inhomogeneity caused by different difference in experimental conditions (section 4.4.2). The main cause for dephasing in diamond NV centres are surrounding paramagnetic impurities in the lattice (e.g. N and ^{13}C atoms) which display dipolar coupling to the NVs. At room temperature, T_2 for nanodiamond NV centres is in the microsecond range. The decoherence time can be improved either by means of lowering the temperature, so that the spin flip process of the spin bath is reduced considerably, or by using samples with lower number of P1 centres [1]. Another pathway is dynamical decoupling, which consists in decoupling the NV spins from their spin bath, for instance by using different pulse sequences [36]. The longest observed decoherence time is 1.8 ms at room temperature for a single NV centre in bulk diamond [6].

3

Coupling nanodiamond NV centres to a superconducting flux qubit

The NV centre can be coupled to other quantum systems like superconducting flux qubits to build hybrid quantum systems. Such a coupling enables us to utilize the advantages of both the sytems for quantum technologies. This chapter discusses the coupling of nanodiamond NV centres to a gap-tunable flux qubit by numerically calculating the coupling constant. The chapter begins with a brief description of the gap tunable flux qubit we considered (section 3.1) and a brief discussion of the achievable coupling constant (section 3.2). Numerical results for the coupling constant are presented in section 3.3. In our calculation, we consider all four possible quantization axes for an ensemble of NV centres in a nanodiamond. We show that coherent strong coupling might be within the reach of present experiments.

3.1 Superconducting flux qubit

A flux qubit is an artificial qubit system constructed using the persistent current states in a micro-meter sized superconducting (SC) loops with a few number of Josephson junctions [37, 38]. The persistent current can be induced in the SC loop by applying an external magnetic flux [37]. It forms a two-level system due to the superposition of left and right rotating persistent currents in the loop. One of the most common flux qubit actually consist of a three Josephson junctions [38] with a fixed gap between the resulting two energy levels. However, adapting different designs and numbers of Josephson junctions, the properties of the two level system can be changed [39, 40].

One can write the Hamiltonian for the two-level system of flux qubit as [41, 42],

$$H_{FQ} = -(\frac{\hbar\epsilon}{2}\sigma_z + \frac{\hbar\Delta}{2}\sigma_x). \tag{3.1}$$

Here, $\hbar$ is the reduced Plank's constant, $\hbar\epsilon$ is the magnetic energy bias of the flux qubit, $\hbar\Delta$ is the coupling energy due to the quantum tunneling of electrons between the two current states and σ_x and σ_z are the Pauli's spin-1/2 matrices in persistent current basis. By diagonalizing equation (3.1), the eigenvalues are found to be $\pm\frac{\hbar}{2}\sqrt{\epsilon^2 + \Delta^2}$. Thus the energy gap of the two level system is $\hbar\sqrt{\epsilon^2 + \Delta^2}$. However, the flux qubit has maximum coherence time at degeneracy point, where ϵ=0, since it is not coupled to the low-frequency noise at this optimal point [43–45].

The gap-tunable superconducting flux qubit considered in this study (figure 3.1) is the one with four junctions presented in references [41, 42]. The energy gap of this flux qubit can be tuned by means of an externally applied magnetic flux. This section reviews very briefly the gap-tunable flux qubit we considered; interested readers can refer to references [41, 42] for a more detailed analysis.

The flux qubit presented in figure (3.1) has two rectangular loops with one inside another and connected symmetrically to the outer loop. The inner rectangular loop with two junctions which are in parallel with each other is known as α-loop. For the outer loop of the flux qubit (figure 3.1), the outer dimensions are $\sim 14 \times 7\ \mu m^2$, the width of the conductor is $\sim 350\ nm$ and thickness of the conductor is $\sim 70\ nm$. A persistent current on the order of I_p ~500 nA is

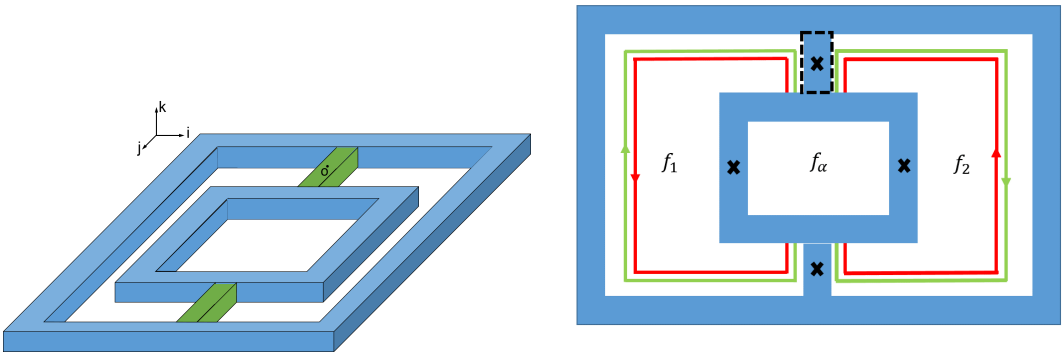

(a) (b)

Figure 3.1: (**a**) Gap-tunable superconducting flux qubit considered in this study. Please see the text for dimensions. The green portion is the superconducting 'bridge' on which the nanodiamond is placed. A small coordinate system (i, j, k) is given with the origin (represented as 'o') at the centre of the bridge. (**b**) Top view of the gap-tunable flux qubit. The black cross mark shows the position of Josephson junctions. The green and red loops with arrows show the left and right circulating currents. The vertical superconducting line with a junction within the black dotted rectangle is the one which we concentrate on this thesis. The diagram is adapted from references [41, 42].

flowing through the lines with junctions outside the α-loop, symmetrically joining the inner and outer loop.

The magnetic energy bias of the flux qubit considered here is basically a measure of magnetic flux in the two halves of the loop and can be written as, $\hbar\epsilon = I_p(f_1 - f_2)\Phi_0$ [41]. Here, Φ_0 is the magnetic flux quantum and f_1 and f_2 are the magnetic fluxes per magnetic flux quantum through the two halves of the loop. The tunnel coupling energy $\hbar\Delta$ and persistent current are tunable by means of the magnetic flux to the α-loop [46]. Going into more detail of this dependence is beyond the scope of this thesis; the interested reader can find more details in references [39, 40]. It is reasonable to consider that the flux qubit at degeneracy point can be brought in resonance with the spin splitting transition of the NV centre when the persistent current is around I_p ~500 nA [41, 42].

3.2 Coupling of the NV centres to the superconducting flux qubit

The magnetic field applied to operate the flux qubit, together with the strain field in the nanodiamond crystal lift the degeneracy of the ground state $m_s = \pm 1$ of the NV centre 2.2.3.

Thus the $m_s = 0$ and $m_s = 1$ form an effective two-level system to which one can couple the resonant flux qubit. The Hamiltonian for this coupled system can be written as,

$$H = H_{NV} + H_{FQ} + H_{int}, \tag{3.2}$$

where H_{NV} is the ground-state Hamiltonian of the electronic spin of the NV centre given in equation (2.1) in section (2.2.3) of chapter (2) and H_{FQ} is the Hamiltonian of the flux qubit given by equation (3.1) in the previous section by setting $\epsilon = 0$. The interaction Hamiltonian can be written as [7, 13, 47],

$$H_{int} = g_e \mu_B \sigma_z \mathbf{B}_{FQ} \cdot \mathbf{S}, \tag{3.3}$$

where, $\mathbf{B}_{FQ}$ is the magnetic field generated by the flux qubit. Considering the fact that the coherent coupling is not possible along the quantization axis of the NV centre [7], which is considered as the z-axis in the present study, the interaction Hamiltonian can be rewritten as [13],

$$H_{int} = g_e \mu_B B_{FQ}^{(x,y)} \sigma_z (S_x \cos\theta_{xy} - S_y \sin\theta_{xy}), \tag{3.4}$$

where $B_{FQ}^{(x,y)}$ is the magnetic field generated by the flux qubit in the x-y plane. θ_{xy} is the angle from the x-axis to $B_{FQ}^{(x,y)}$ in the x-y plane which depends on the position of the NV centre. The strength of the coupling of a single NV to a flux qubit is $g = g_e \mu_B B_{FQ}^{(x,y)}$.

On the other hand, if an ensemble of NV centres with the same crystallographic orientation are coupled to the flux qubit, each of the NV centres in the ensemble would have slightly different coupling strengths. One can show that, the individual coupling strengths couple to give a total coupling strength for the ensemble case of $G = (\sum_n g_n^2)^{1/2}$ [7].

3.3 Coupling nanodiamond NV centres to gap-tunable flux qubit

Previous studies of coupling NV centres in diamond to flux qubits, use approximately 10^7 spins in bulk diamond to achieve strong coupling [7, 10, 11]. Instead of using a large number of spins, the coupling strength can also be increased by increasing the magnetic field at the

point where the NV centre is located. This can be achieved by placing the individual NV centres closer to the superconducting line of the flux qubit [7]. The present study therefore considers nanodiamonds instead of bulk diamond, since the diamond nanocrystals can be placed exactly on the superconducting bridge of the gap tunable flux qubit presented in figure 3.1. One important thing to note here is that the present study considers the ensemble case where the number of NV centres along the four crystallographic orientations are the same. Thus the coupling of each sub-ensemble is independent from each other as the quantization axes are different [7].

3.3.1 Strength of the coupling

The NV centres are randomly distributed inside the nanodiamond which is assumed to be spherical for simplicity. When we place the nanodiamond crystal in the vicinity of the flux qubit, each NV centre would experience a (slightly) different coupling strength. Thus we need to calculate the coupling strength for the total ensemble. Here, we compute the average total coupling strength in a nanodiamond which would be consistent with what is measured in experiments.

Usually, in nanodiamonds, NV centres are not stable near the surface. In our nanodiamonds, for simplicity of the calculation, we assume the ensemble of stable NV centres to be cubical in shape and with its side located $\sim D/20$ distance from the surface of the spherical crystal with diameter D (the cross-section of the nanodiamond crystal on the flux qubit is given in figure (3.2)). The assumption is more or less consistent with a previous measurement performed in the lab [48], but it is not one hundred percent correct-especially it overestimates the number of NVs for very small nanodiamonds and underestimates in for largest ones.

Let us consider the quantization axis of the NV centre as the z-axis, then the strength of the coupling is determined by the magnetic field in the x-y plain, which is, $B^{(x,y)} = \sqrt{B_x^2 + B_y^2}$. Then the magnetic field component $B^{(x,y)}$ at the centre of each small cube determines the average coupling strength in that cube. Usually the NV centres in the nanodiamond are distributed among the four possible quantization axes. This has to be taken into account when considering the number of NV centres for coupling. Thus only one of the sub-ensembles with one quarter of the total number of NV centres in a single nanodiamond will take part

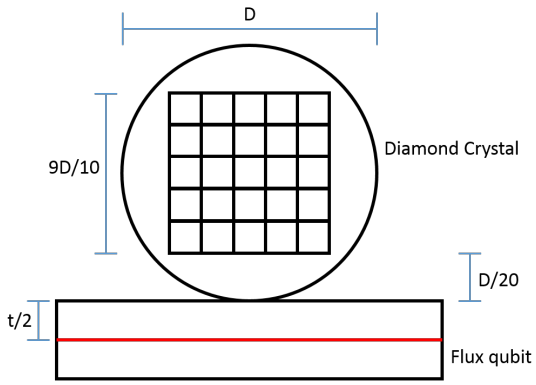

Figure 3.2: Cross-section of a spherical nanodiamond crystal placed on the superconducting bridge connecting the inner and outer loop, within the black dotted rectangle in figure (3.1b). The rectangles inside the circle represent the ensemble of NV centres subdivided into small cells, the red line represent the centre of the superconductor, for calculating the magnetic fields using Biot-Savart law. The thickness t of the superconductor is 70 nm and the diameter of the diamond crystal is denoted as D.

in the coherent collective coupling. As a result the coherent collective coupling of each sub-ensemble can be given as,

$$G = \left(\sum_{m} \frac{\text{No.of NV centres in the crystal}}{4 \times \text{No.of small cubes}} g_m^2 \right)^{1/2}. \tag{3.5}$$

Here g_m is the coupling constant at the centre of the mth small cube. One point to note here is that the NV centres are distributed randomly in the cubical ensemble and the numerical calculation we present here gives an average of all the possible random distributions.

3.3.2 Random orientation of the nanodiamond NV centres

The challenge involved in working with the nanodiamond is the random orientation of the quantization axis. Unlike in bulk diamond, it is very tricky to precisely fix the quantization axis along a desired direction for nanodiamonds, while performing experiments. Thus we have to consider a randomly oriented coordinate system where the magnetic field components $B^{(x,y)}$ vary based on the orientation of the quantization axis. To account for the random orientation of the quantization axis, we can convert the x and y magnetic field components in spherical polar coordinates. Let us consider the four possible quantization axes in the diamond lattice as z_1, z_2, z_3 and z_4 (shown in figure 3.3a) and the magnetic field in the coordinate system of one of the quantization axes, for instance, z_1 (shown in figure 3.3b).

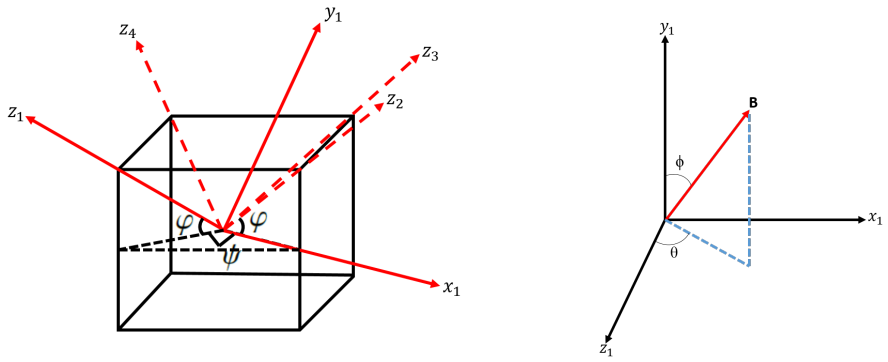

(a) (b)

Figure 3.3: (**a**) Four possible quantization axes in the diamond lattice denoted by z_1, z_2, z_3 and z_4. Coordinate system of one of the quantization axes z_1 is shown. (**b**) Magnetic field vector in the coordinate system of quantization axis z_1. The angle made by the magnetic field vector **B** with y_1 is ϕ and the angle made by the projection of **B** in the (x_1, z_1) plain with z_1 is θ.

The magnetic field generated by the flux qubit at an arbitrary point with respect to the co-ordinate system of z_1 can be written as,

$$\mathbf{B}_1 = \begin{bmatrix} B\sin\theta\cos\phi \\ B\cos\phi \\ B\cos\theta\cos\phi \end{bmatrix} \tag{3.6}$$

Rotating the co-ordinate system of the quantization axis z_1 by an angle φ=$\cos^{-1}\sqrt{\frac{2}{3}}$ counter-clockwise with respect to x_1, ψ=$\frac{\pi}{2}$ counter clockwise with respect to y_1 and φ clockwise with respect to x_1 will give the co-ordinate system of quantization axis z_2. If we rotate by ψ=π or $\frac{3\pi}{2}$, the coordinate system of quantization axes z_3 and z_4 can be reached. Please note that only the coordinate system of quantization axis z_1 is shown in the figure (3.3a). Moreover, the other three co-ordinate systems can be reached by different sequence of rotations and here we present only one of those sequences as we can study the random rotation with this one possible case.

In the present case, the magnetic field vector is actually constant and the coordinate system is randomly oriented. However, this case is equivalent to the case where the co-ordinate system is constant and the magnetic field is randomly oriented. This means that θ and ϕ can have any values from [0, 2π] and [0, π], respectively. $|\mathbf{B}_1|$ can be calculated by considering any direction for the z_1 axis. We calculate this by considering the z_1-axis parallel to the

portion of superconducting line we are considering in the present study (green color portion in figure 3.1a). The expression for the three components is given in the section A.1 of the Appendix.

The magnetic field components of equation 3.6 are given with respect to one of the four sub-ensembles with quantization axis z_1. However, the other three sub-ensembles can also be coupled to the flux qubit and the coupling of each sub-ensemble should be independent of each other as the quantization axes are different. Thus it is important to calculate the coupling strengths of the other three sub-ensembles as well. For this, we can write a general expression for the magnetic field vector with respect to all the four coordinate systems by using rotation matrices as,

$$\mathbf{B}_j = R_x(-\varphi)R_y(\psi)R_x(\varphi)\begin{bmatrix} B\sin\theta\cos\phi \\ B\cos\phi \\ B\cos\theta\cos\phi \end{bmatrix}, \tag{3.7}$$

where the index j =1, 2, 3, 4 represents the coordinate system defined by the quantization axes of the four sub-ensembles, respectively. The rotational matrices R_x and R_y are given by,

$$R_x(\varphi) = \begin{bmatrix} 1 & 0 & 0 \\ 0 & \cos\varphi & \sin\varphi \\ 0 & -\sin\varphi & \cos\varphi \end{bmatrix} \quad , \quad R_y(\psi) = \begin{bmatrix} \cos\psi & 0 & -\sin\psi \\ 0 & 1 & 0 \\ \sin\psi & 0 & \cos\psi \end{bmatrix} \tag{3.8}$$

3.3.3 Numerical calculation of the coupling strength

We begin the numerical estimation by considering the nanodiamonds containing ensembles of NV centres, since for a single centre case, the coupling strength can only be in the kHz range, which is too low to reach strong coupling. The size of the nanodiamond crystal we are dealing with has diameters ranging from 10 nm to (150±50) nm. In the nanocrystals, there are 300 parts per million N atoms and the conversion ratio between NV to N is roughly 1:10 [49]. Thus the number of NV centres in our nanodiamonds can be calculated as $\sim 3.53 \times 10^5 \times D$, where D is in nanometer. Using the scheme discussed in section (3.3.1), we calculate the collective coupling strength for different sizes of nanodiamonds with sub-ensembles of all four quantization axes; the results are shown in figure (3.4).

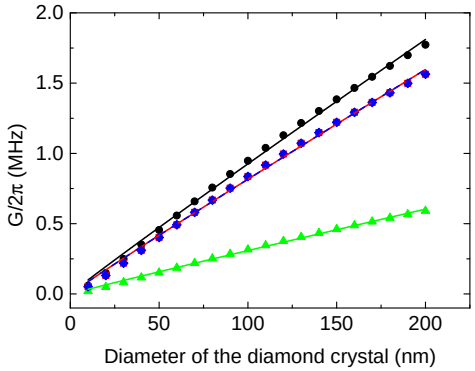

Figure 3.4: Collective coupling strength for the four sub-ensembles as a function of diameter of the nanodiamond. The black, green, blue and red lines correspond to sub-ensembles with quantization axes z_1, z_2, z_3 and z_4, respectively. The points are numerically calculated and the curve for each sub-ensemble is the best fit of the form $\propto D^{0.97}$.

Here we have assumed that the centre of the nanodiamond is centred above the superconductor bridge, where the height of the centre is equal to the radius of the nanodiamond, and both θ and ϕ are arbitrarily considered as zero. Since the number of NV centres is proportional to the cube of the diameter, one would expect a non-linear increase in the coupling strength (very naively $D^{3/2}$). However, the fits shown in figure 3.4 demonstrate that when the size of the nanodiamond increases the coupling strength is almost linearly proportional to the diameter of the crystal ($\propto D^{0.97}$). This can be interpreted considering that the increase in the number of NVs leads to an increase in the coupling strength, which is however compensated by the decrease in the strength due to the increase in their distance from the flux qubit.

Next we try to find the tolerance in precise positioning of the nanodiamond on the superconducting bridge. For this we can consider the position of the centre of nanodiamonds with respect to a reference point on the superconductor part at the centre both in width and length (represented in a small coordinate system in figure 3.1a). It is straightforward to see that when the height of the centre increases the coupling strength decreases as the magnetic field lowers when the nanodiamond rises up from the conductor. We plot coupling strength along the i-axis and j-axis for nanodiamond of diameter 150 nm, assuming $\theta = 0$ and $\phi = 0$ for all the four sub-ensembles. The results are shown in figures 3.5b and 3.5a.

As one would expect from the symmetric considerations, the figure 3.5 shows that the coupling strength is maximum at the centre of the bridge. We can see From figure 3.5b that

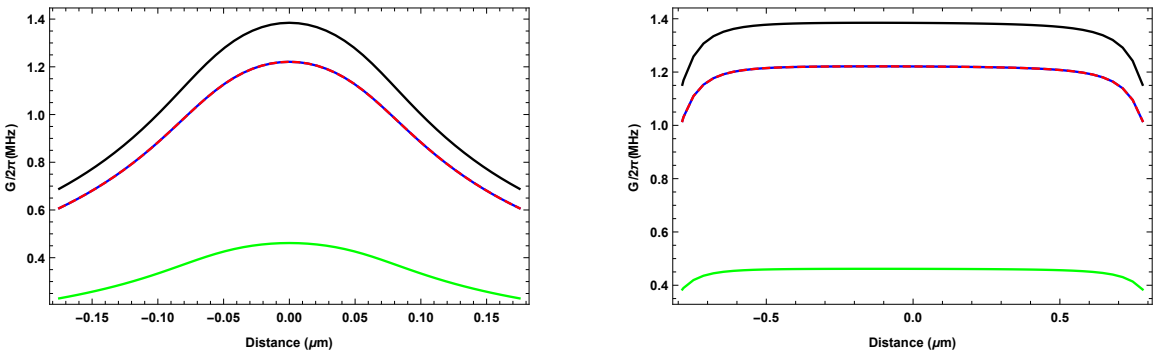

(a) (b)

Figure 3.5: Collective coupling strength for all the four sum-ensembles in a nanodiamond of diameter 150 nm, along the i (**a**) and j (**b**) directions. Here we consider the origin of the coordinate system to be at the centre of the top plane of the superconducting bridge (see figure 3.1a). The solid black, solid green, solid blue and dashed red curves in both the figures correspond to sub-ensembles with quantization axes z_1, z_2, z_3 and z_4, respectively.

the tolerance in precise positioning along the i-direction is around 1 μm and from figure 3.5a, the tolerance is of the order of 20 nm. With the nano-tweezers in the scanning electron microscope (SEM) locally available at Macquarie University (JEOL JSM-6480), one can achieve precise positioning within ~10 nm. Thus using existing technology we can precisely position the nanodiamond, for maximum coupling.

Now we consider the random orientation of the NV centres in the nanodiamonds. We pick the optimum size of 150 nm and assume the nanodiamond to sit exactly on the superconductor near the centre of the bridge. However, this optimizations does not guarantee enough coupling strength as the quantization axis can be randomly oriented. To analyse it we estimate the ensemble coupling strength for the nanodiamond of optimum size, placed at optimum position for all the possible values of θ and ϕ considering all the four sub-ensembles with orientations z_1, z_2, z_3 and z_4. The results are shown in figures (3.6a), (3.6b), (3.6c) and (3.6d).

In all the four possible orientations the ensemble coupling strength can vary from 0 to ~1.4 MHz. This indicates that if we have only one of the sub-ensemble, we can have any of the coupling strength between 0 and ~1.4 MHz. Suppose we are obtaining a very low coupling strength of a few kHz coupling strength, one can optimize the coupling strength by rotating the orientation of the quantization axis, by means of rotating the whole diamond nanocrystal. Experimentally, it is very difficult to rotate the nanodiamond in a desired direction. Also we would not know in which direction we would have to rotate it as the quantization axes

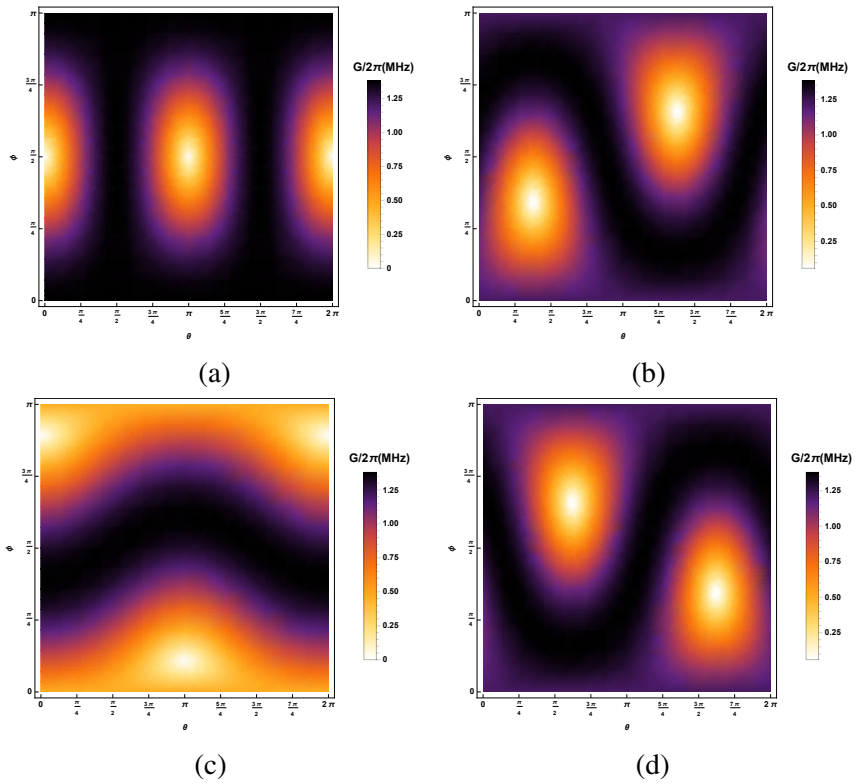

Figure 3.6: Collective coupling strength of a nanodiamond of diameter 150 nm, for all the possible orientations (for all possible ϕ and θ) placed on the super conductor grid, with the centre of the crystal above the centre of the grid both in length and width (**a**) sub-ensemble with quantization axis z_1 (**b**) sub-ensemble with quantization axis z_2 (**c**) sub-ensemble with quantization axis z_3 (**d**) sub-ensemble with quantization axis z_4

are randomly oriented. While we have all the four sub-ensembles in the crystal, each of them will independently couple to the flux qubit system as the orientation of each of their quantization axis is different. Interestingly, from figure 3.6 one can see that for any value of θ and ϕ at least one of the four sub-ensembles will have an appreciable amount of coupling strength, $G/2\pi$. To understand that, we plot the maximum coupling strength among the four orientations (figures (3.6a),(3.6b), (3.6c), (3.6d)) at each θ and ϕ values and the result is shown in figure 3.7.

This plot indicates that irrespective of the orientation of the crystal, we achieve a minimum coupling strength of 1.24 MHz. One can achieve a coherence time of the flux qubit ($1/T_2^{FQ}$) up to a few micro-seconds. Thus a dephasing rate of the flux qubit is smaller than $\eta/2\pi \sim 1$MHz can be achieved (were $\eta/2\pi = 1/T_2^{FQ}$) [50, 51]. The coherence time of NV centres (T_2^{NV}) increases considerably with a decrease in temperature. Previous studies given in [52] report a huge increase in the coherence time of up to ~250 μs at temperatures below 2 K from a room

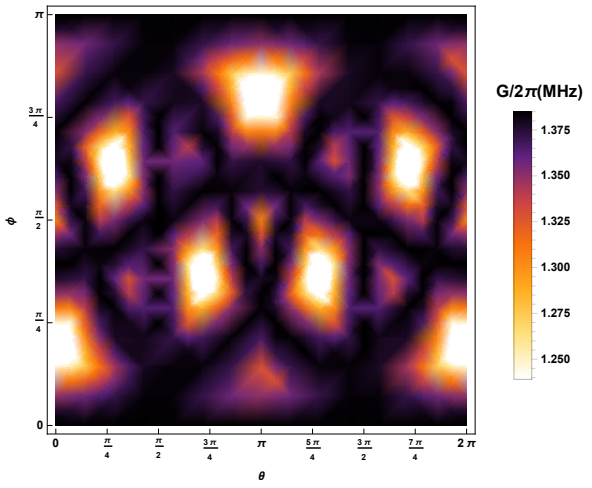

Figure 3.7: Maximum coupling strength among the four sub-ensemble in a randomly oriented nanodiamond given in figures (3.6a),(3.6b), (3.6c), (3.6d).

temperature value of ~6.7 μs. This increase in coherence time is due to the complete spin bath polarization (99.4%), resulting in a complete decoupling from the fluctuating magnetic field generated by the spin flip-flop process. Since the flux qubit's working temperature is $\sim 10mK$, one can expect that NV centres are effectively decoupled from the spin bath. Later on in chapter 5, we shall experimentally determine the coherence time of a single NV centre in a nanodiamond to be ~3.7 μs. At flux qubit's working temperature, it is reasonable to expect a coherence time greater than 10μs. Thus the dephasing rate of $\kappa/2\pi = 1/T_2^{NV}$ is smaller than 0.1 MHz. Then the coupling strength $G/2\pi$ is greater than both $\kappa/2\pi$ and $\eta/2\pi$ and the cooperativity parameter $\frac{G^2}{\kappa\eta}$ is greater than ~15 [53]. This implies that a coherent transfer of quantum information is possible between the flux qubit and the NV centre. However, there is one restriction on coherence times from the NV centre point of view and that is the inhomogeneous broadening of the zero-field splitting due to the strain field [54]. Even at the temperature of the flux qubit, the strain field would be present in the diamond nanocrystals. Studies presented in reference [55] show, that the strain broadening can be as large as a few MHz, which is on the order of $G/2\pi$. This inhomogenous strain induces a slight difference in the ground state spin transitions. Thus the NV centre transitions would not be identical, leading to additional dephasing. At present there is no such study on the inhomogenous strain field broadening available in literature. A proper characterization of the NV centres in the nanodiamond is needed to produce a meaningful estimation. This is one of the directions we plan to pursue in the future. We anticipate that a careful 'hard' selection of an 'ideal' nanodiaond with as small a strain splitting as possible will be needed.

4

Experimental methods and setup

This chapter describes the experimental methods and setups that we used to perform coherent spin manipulation with MW fields. We begin with a discussion about the sample containing NV centres (section 4.1), then we describe the lab-built confocal microscope (section 4.2) and Hanbury-Brown and Twiss interferometer for detecting single emitters (section 4.3). The ODMR measurements are presented in section 4.4. Finally we discuss the two different methods for applying MW fields to the NV spins in section 4.5. Emphasis is put onto a new method based on a dielectric MW cavity, which was developed within our research group (section 4.5.2). The cavity allows uniform and large scale application of MW radiation unlike conventional methods.

4.1 Nanodiamond sample containing NV centres

The nanodiamonds we used in our characterization are synthetic, high pressure high temperature (HPHT), type Ib powders (N concentration > 20 ppm) with a nominal average

size of 100 nm (MSY< 0.1 μm; Microdiamant). A suspension of desired concentration is prepared by diluting the nanodiamond powder in deionized water (Milli-Q). We put a few drops of the prepared suspension on to a glass coverslip (18 $\times$ 18 mm^2 and thickness ~0.13-0.17 mm; Menzel-Glaser) and allow it to dry. The nanodiamonds hence lay on top of the glass cover slip; we use a laser beam focused on the 'nanodiamonds-plane' from the bottom of the sample for optical characterization. In addition, an Atomic Force Microscope (AFM) is mounted above the sample in order to simultaneously measure the size of the nanodiamonds. As a new experimental direction in the research group, this thesis study single NV centres. However, in the future we are planning to extend our studies towards the ensemble cases for the coupling to the flux qubits. While ultimately we will look into ensembles of NV centres to couple to the flux qubit, the study of single NV centre is still relevant as at room temperature the inhomogeneous magnetic fields generated by the spin bath is effectively reduced.

4.2 Lab-built confocal microscope

We use a lab-built confocal microscope to precisely locate the nanodiamonds from the sample, by tracing their fluorescence. The schematic diagram of our lab-built confocal microscope is shown in figure 4.1.

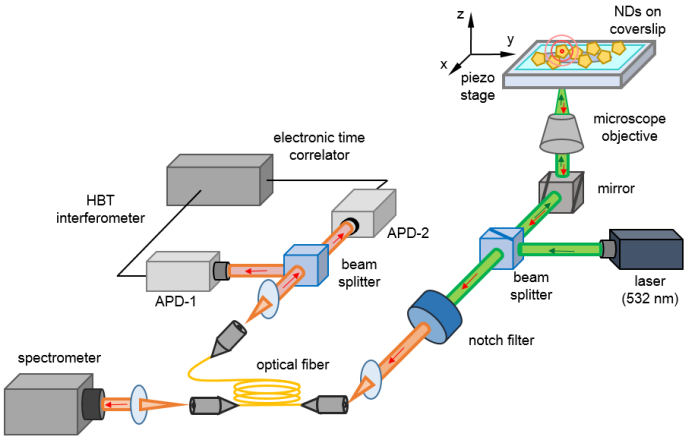

Figure 4.1: Schematic representation of the lab-built confocal microscope and its detection setup. The green arrow represents the excitation laser and the red arrow represents the fluorescence light from the NV centres. The detection path includes a spectrometer and a HBT interferometer.

The laser used in our setup is a temperature-controlled (LTC100-A; Thorlabs), continuous wave, 532-nm diode-pumped solid-state (DPSS) laser diode (DJ532-40; Thorlabs). It is used in combination with a free-space optical isolator (IO-5-532-HP, Thorlabs) mounted after the laser output to minimize back-reflected optical feedback and thus prevent mode hopping, amplitude modulation and frequency shift of the source.

We direct the laser towards a beam splitter, which is a mirror blank (PF20-03;Thorlabs). The diagonal plane of the beam splitter kept at 45° towards the sample holder, reflects 10% of the light from the excitation source towards the sample and transmits 90% of the fluorescence from the NV-nanodiamond sample towards the detection path. The beam is then focussed on the sample through the transparent glass cover slip, from the bottom using a mirror kept at 45° upwards and a microscope oil objective (UPlanFL N, 100×/N. A. 1.3 / W. D. 0.2 MM / F. N. 26.5; Olympus). The laser excites the NV centres in the nanodiamonds within the focusing area and NV centre fluorescence is detected. The piezoelectric stage on which the glass cover slip is mounted is part of our room temperature AFM platform (SMENA; NT-MDT) which is used for the size determination of the nanodiamonds. The piezoelectric stage has a controlled movement in x and y direction of 50×50 μm^2, in a minimum scanning step of 6 pm. This enables the scanning of the whole sample, literally, point by point. In addition, the microscope objective can be moved several millimeters by means of a micrometric screw for coarse alignment. The stage itself allows fine adjustment over a travel range of 10 μm along z direction to achieve the optimum focusing of the laser beam.

The fluorescence of the NV centres is collected by the microscope objective and 90% of that light is transmitted through the beam splitter. The transmitted light beam reaches the notch filter (NF-533-17; Thorlabs), which filters the NV emission and blocks unwanted excitation light reflected from the glass cover. The filtered NV emission is then coupled to a single mode optical fibre (P3-4608-FC-5; Thorlabs). The fibre works as a pinhole, which helps to eliminate all out-of-plane fluorescence and delivers, the light either to the spectrometer or the HBT interferometer located across the table for optical characterization of the NV fluorescence.

The detection apparatus has two parts. The first one is the spectrometer (SpectraPro Monochromator Acton SP2500, with a Pixis Camera model 7515-0001; Princeton Instruments), which collects the fluorescence, analyses and provides the spectrum. The NV fluorescence is also captured by a Hanbury-Brown and Twiss (HBT) interferometer, which is used to analyse the photon correlation properties of the NV centre. Furthermore, any of the two avalanche photodiode (APD) (SPCM-AQR-14; Perkin Elmer) can be used to monitor the NV fluorescence over time for lifetime measurements or for performing optically detected magnetic resonance (ODMR).

4.3 Hanbury-Brown and Twiss interferometer

The Hanbury-Brown and Twiss (HBT) interferometer is shown in figure (4.2a). We use this to detect the nanodiamonds containing single NV centres via autocorrelation measurements [1, 56, 57].

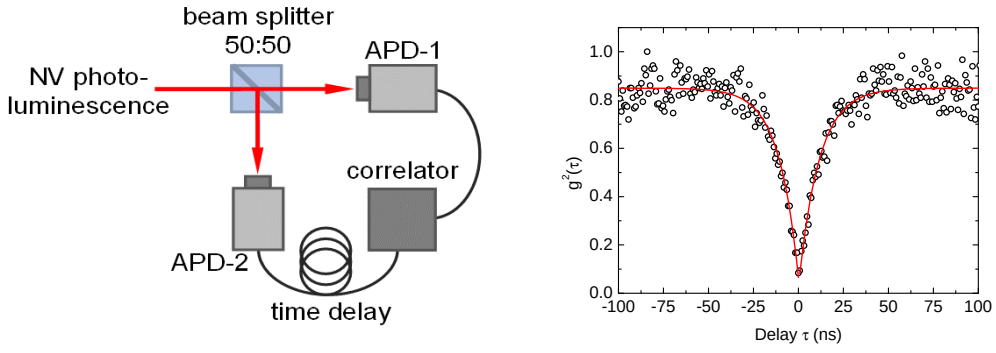

(a) (b)

Figure 4.2: (**a**) Schematic representation of the HBT interferometer. The 50:50 beam splitter equally transmits and reflects light to two APDs in their respective paths. The APDs are connected to the correlator. A variable time -delay is introduced via an additional BNC cable in the stop path. (**b**) An anti-bunching curve for a single NV centre measured in our lab. The contrast of the dip is more than 80%.

Our HBT interferometer consists of a 50:50 beam splitter (BSW10; Thorlabs) to split the NV centre fluorescence into two arms and redirects it onto two separate APDs. The correlator is a time-correlated single-photon counting system (PicoHarp 300, channel width 4 ps, with digital and analog units PH 300; PicoQuant) which measures the second order correlation function $g^{(2)}(\tau) = \frac{\langle I(t)I(t+\tau)\rangle}{\langle I(t)^2\rangle}$, where $I(t)$ is the intensity detected by the APDs

at time t. The quantity $g^{(2)}(\tau)$ is the conditional probability of detecting a photon at time $t + \tau$ provided a photon was detected at t, averaged over all t. Thus for a single centre, when $\tau \to 0$, $g^{(2)}(\tau) \to 0$, shows the characteristic anti-bunching dip of a single photon (or quantum emitter) (figure 5.3a). From $g^{(2)}(\tau = 0)$ and the contrast of the anti-bunching dip, one can estimate the number of NV centres in a given nanodiamond, as the contrast scales inversely proportional to the small Number of NV centres [1].

4.4 Optically detected magnetic resonance

The spin physics of the NV centre can be studied by coupling it to a resonant MW field and performing optically detected magnetic resonance (ODMR) measurements. ODMR measurements can be done in two ways, continuous-wave ODMR and pulsed ODMR.

4.4.1 Continuous-wave ODMR for identifying the resonant MW field

Continuous-wave ODMR measurements are performed by applying both laser and MW field excitation continuously, on a single NV centre. The continuous application of the laser beam polarizes the NV centre in the $m_s = 0$ state, resulting in maximum fluorescence from the NV centre. To identify the exact resonant frequency between the ground state $m_s = 0$ to $m_s = \pm 1$, we sweep the MW frequency around the typical value for the ground-state zero field splitting of the NV centre in diamonds (~2.87 GHZ). When the MW frequency hits the resonant value, we observe a drop in the emission from the centre as the NV spin is driven from the 'brighter' $m_s = 0$ state to the 'darker' $m_s = \pm 1$ (see section 2.3.1). Ideally, one should only observe one resonant frequency. However, when stress in the diamond lattice is present or there is an external magnetic field, two resonant frequencies can be observed, since the $m_s = \pm 1$ degeneracy will be lifted in both cases, resulting in two distinct resonant frequencies. This property can actually be exploited to detect and measure the intensity of external magnetic fields by measuring the difference between two frequencies. A detailed description of such measurement techniques is however beyond the scope of this thesis and the interested reader is referred to reference [19].

4.4.2 Pulsed ODMR for spin manipulation and spin-echo studies

The spin manipulation with Rabi oscillation and spin-echo measurements can be done with pulsed ODMR. Pulsed ODMR measurements use time-pulsed sequences for both microwave and laser. The first step in pulsed ODMR measurements is the generation of both MW and laser time-pulsed sequences.

Pulse generation

To produce the laser- and microwave-timed sequences we use a TTL signal generator (Pulse Blaster; Spincore Technologies Inc) with 10 ns pulse resolution at 100 MHz. In order to control the excitation laser and shape the desired pulses, we send it through an acousto-optic modulator (AOM) in a double-pass configuration (figure (4.3)) [58], before it is delivered to the sample.

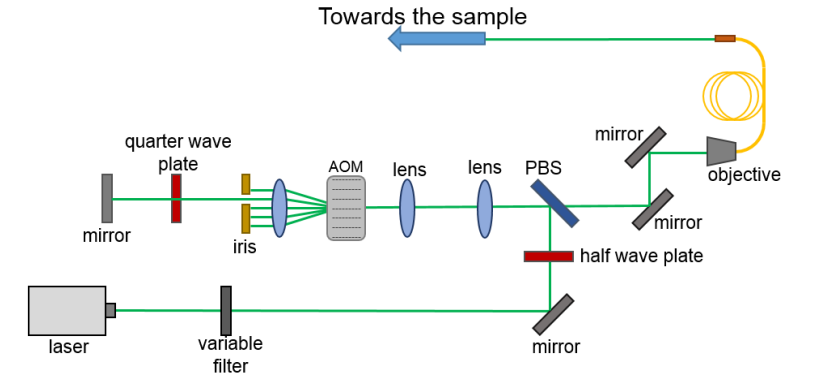

Figure 4.3: Top view of the laser pulse generation setup in a double pass AOM configuration. The output is sent towards the sample.

The linearly polarised laser beam from the source passes through a circular, continuously variable metallic neutral density filter (NDC-25C-2M;Thorlabs) to coarsely adjust the laser power. We do not employ an active electronic feedback loop at this stage, as we use AOM as a 'switch'. A combination of a half-wave plate (WPH05M-532; Thorlabs) and a polarizing beam splitter cube (PBS 102 Thor labs) allows for the adjustment of the optical power in the AOM arm. The beam is passing through the AOM after being adjusted in size by two lenses in a Kepler telescope configuration. The AOM, is powered by its RF driver, which is time-gated by the TTL signal from the signal generator. The AOM allows the laser beam to pass through it unaffectedly when it is in 'off' and diffract the laser beam into different

orders, when it is 'on'. The lens kept after the AOM collimates the diffracted orders and the iris filters the first. The first order diffracted then passes through the quarter-wave plate twice: before and after being reflected by the mirror so that the polarization axis is rotated by 90^0. Thus the reflected laser beam is fully transmitted through the PBS and is delivered to the sample (section 4.2) by means of a single optical fibre.

Spin manipulation with Rabi oscillations and spin echo measurements

The time-pulsed sequences of both laser and MW for the Rabi oscillation measurement are shown in figure 4.4a. The NV centre is initialized to the $m_s = 0$ ground state with an off-resonant laser pulse (see section 2.3.1). Then the MW pulse, which is in resonance with the splitting of the ground state $m_s = 0$ and $m_s = \pm 1$ is turned on to drive and manipulate the spin state of the NV centre (see section 2.3.2 for more details on the manipulation with Bloch sphere representation). The detection of the spin state is done with a laser pulse after turning off the MW pulse, as the fluorescence of the NV depends on the state the spin is in, i.e. 'brighter' in $m_s = 0$ and 'darker' in $m_s = \pm 1$.

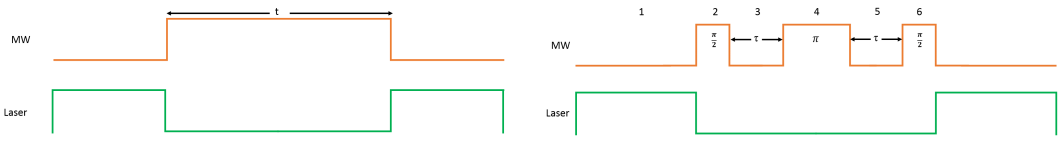

(a) (b)

Figure 4.4: (**a**) Pulse sequence of both the laser and MW for the Rabi oscillation measurements. (**b**) Pulse sequence of both the laser and MW for the spin-echo measurement.The green pulses and the orange pulses correspond to the laser (532 nm) and MW, respectively. For the spin-echo measurements, each step is represented as 1, 2, 3, 4, 5 and 6.

From the Rabi measurement, we determine the duration of the π-pulse to drive the $m_s = 0 \leftrightarrow m_s = \pm 1$ transition. We then can design the pulse sequence for the spin-echo measurement. The time-pulsed sequence of both laser and MW for the spin-echo measurement is shown in figure 4.4b, the corresponding Bloch sphere representation is given in figure 4.5.

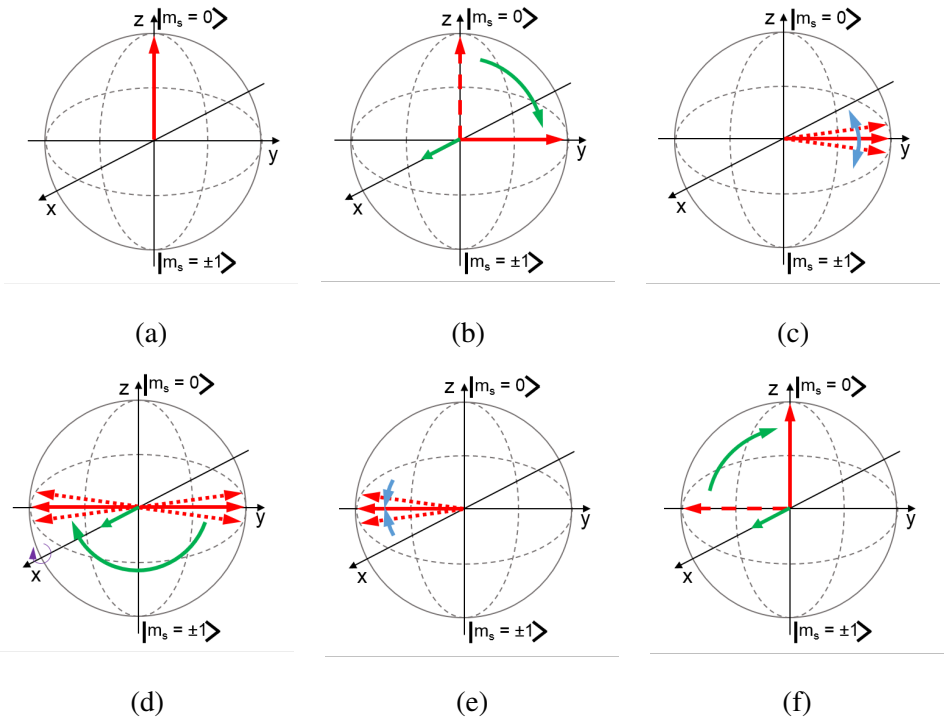

Figure 4.5: Bloch sphere representation of spin-echo pulse sequence. (**a**) The spin state of the NV centre is initialised to $m_s = 0$ by the excitation of the laser pulse. (**b**) The application of an applied MW $\frac{\pi}{2}$ pulse drives the system in to a superposition state. The green curved arrow represents the Larmor precession direction due to the MW (green straight arrow). (**c**) Dephasing due to free precession in the superposition state. The curved blue arrows represent the direction of precession. (**d**) Application of π pulse to induce re-phasing. (**e**) Free precession and refocussing the spin state. (**f**) Re-projection of the dephased superposition state to the $m_s = 0$ state by applying a $\frac{\pi}{2}$ pulse.

The laser pulse (step 1 of figure 4.4b) initializes the NV centre spin in the $m_s = 0$ ($|0\rangle$) ground state (Bloch sphere representation in figure 4.5a). After the initialization pulse, three microwave pulses are applied 'in the dark' (i.e. with laser off) along the x direction in the Bloch sphere, which causes Larmor precession of the spin state about the x-axis. First we apply a $\frac{\pi}{2}$ pulse (step 2 of figure 4.4b), which takes the spin state from $|0\rangle$ to the superposition state $\left|\Psi_{sp}\right\rangle = \frac{1}{\sqrt{2}}(|0\rangle + e^{i\phi_{ph}}|1\rangle$ (Bloch sphere representation in figure 4.5b; where $|0\rangle$ represents the $m_s = 0$ and $|1\rangle$ represents the $m_s = \pm 1$). Then the MW is turned 'off' for a time period of τ (step 3 of figure 4.4b). The spin in the superposition state dephases by undergoing a free evolution and accumulating a phase ϕ_{ph} (Bloch sphere representation in figure 4.5c). Applying a π pulse along the x-axis (step 4 of figure 4.4b), the superposition state undergoes a flip to the state $\left|\Psi_{sp}\right\rangle = -\frac{1}{\sqrt{2}}(|0\rangle - e^{i\phi_{ph}}|1\rangle$ by an angle π in the Bloch sphere (figure 4.5d). The spin undergoes a free evolution in step 5, in opposite direction to the free

evolution of step 3 and thus refocuses the dephasing caused by the low frequency noises, which are basically local noise fields (Bloch sphere representation in figure 4.5e). Finally on applying a $\frac{\pi}{2}$ pulse (step 6 of figure 4.4b), the spin state re-phases back to the $|0\rangle$ state (Bloch sphere representation in figure 4.5f). An optical read-out of the NV spin state can be taken with a laser pulse, by measuring the intensity of the NV's fluorescence. This informs us on the dephasing caused by the homogeneous noise (section 2.4).

4.5 Applying MW field to the NV centre

We generate the MW field which is coupled to the NV centre via two different methods. The first is the standard on-chip micro-wire technique, while the second employs a MW cavity, which is a new method devised within our group [14].

4.5.1 On-chip micro-wire

We apply the MW to the nanodiamond sample via a copper wire with diameter of ~20 μm, which is in direct contact with the nanodiamond sample and acts as a MW antenna (figure 4.6). The MW signal sent down the wire (power in the range of 0.2-0.6 mW) is generated by a signal generator (SMIQ 06B, 300 kHz to 6.4 GHz; Rohde & Schwarz) and amplified with a MW amplifier (ZHL-16W-43+; Mini-Circuits). Due to the net field drop off of the H-field around a current carrying wire, the wire has to be very close (~ tens of μm) to the sample, in order to efficiently deliver the MW.

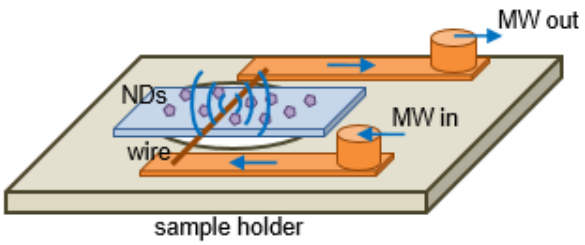

Figure 4.6: Schematic representation of the on-chip micro-wire for the MW supply. The diameter of the wire is ~20 μm and it is ~tens of μm away from the sample.

4.5.2 Dielectric MW cavity

The newest, original method we use to supply the MW to the NV centre employs a MW cavity with cylindrical symmetry, loaded with a dielectric material, designed within our group [14] (figure 4.7).

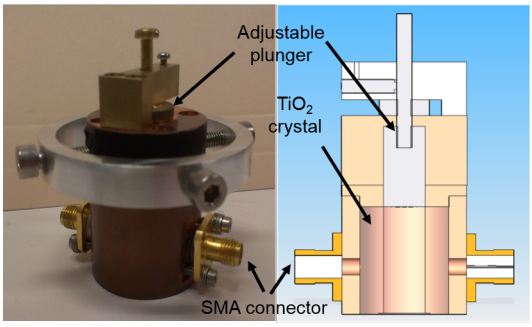

Figure 4.7: Picture and schematic representation of the dielectric MW cavity. The dielectric material is TiO_2. The outer length and height of the cavity are 32 mm and 20 mm, respectively.

Unlike the micro-wire, the cavity is able to address sample areas over a large, macroscopic range (MW confinement is 10×10 mm^2 area). The outer diameter of the cavity is ~32 mm and the height is ~20 mm. Let the symmetry axis of the cavity be z'. The cavity has a pure transverse electric mode (TE mode) with magnetic field components along the symmetry axis ($H_{z'}$) and also along the radius (H_r). Compared to other MW cavity designs such as whispering gallery mode, the TE mode shows less confinement to the dielectric and reaches higher Q-factor (~1000 in our case), as the spurious modes are less [59]. The dielectric material inside the cavity is TiO_2, since it has high permittivity, low MW loss and, most importantly, has a fundamental mode frequency of ~2.2 GHz, which is close to the zero field splitting of the NV centre ground state. We can represent the modes of the cavity in terms of the number of azimuthal modes ($2m$), number of radial modes (n) and number of symmetry axis modes (p), as $TE_{m,n,p}$. However, we have m= 0 for a pure TE confinement, and thus we can define the three different modes of interest as $TE_{0,1,1}$, $TE_{0,1,2}$ and $TE_{0,1,3}$. The cavity is designed with an adjustable plunger, which can tune the cavity frequency of each mode. The tuning of the cavity frequency for each of the three modes is shown in figure 4.8a as a function of plunger position.

From the numerical simulation given in figure 4.8a, it can be seen that the $TE_{0,1,3}$ mode of the cavity can be mechanically tuned in to resonance with the NV centre and thus we

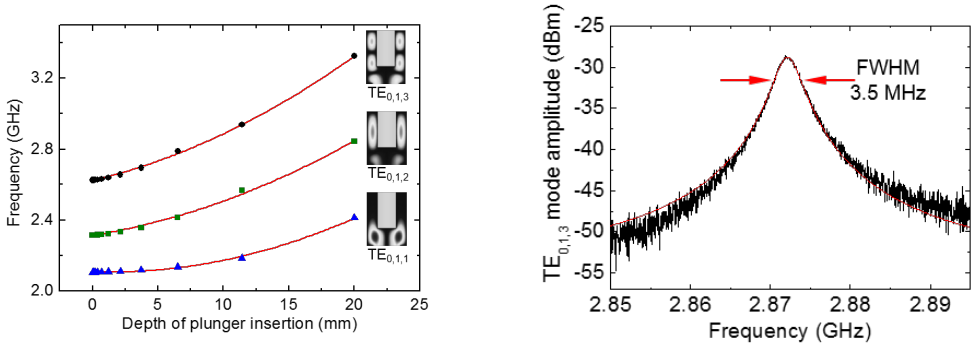

(a) (b)

Figure 4.8: (**a**) Transverse electric mode frequencies based on numerical simulation for different plunger positions. (**b**) Transmission spectrum for the $TE_{0,1,3}$ mode of the MW cavity recorded with the Fieldfox N9918A. The peak shows the resonance frequency of the cavity and the Full-Width at Half-Maximum (FWHM) is ~3.5 MHz [14].

consider this mode for the MW coupling. The transition spectrum of the $TE_{0,1,3}$ mode of the cavity was recorded with a Fieldfox N9918A (Aglient Technologies) and it is shown in figure 4.8b. The peak shows the resonance frequency of the cavity in $TE_{0,1,3}$ mode, tuned around the desired value of 2.87 GHz.

The magnetic field components along the radius and along the symmetry axis are an important factor in the coupling of MWs to the NV centres. We can analyse the magnetic field components as a function of height above the bottom edge of the cavity along the z'-axis and also along the radius from the symmetry axis by plotting a density plot for both H_r (figure 4.9a) and $H_{z'}$ (figure 4.9b). To find the optimum position along the radius from the symmetry axis, we can plot a two-dimensional plot of H_r (figure 4.9a) and $H_{z'}$ (figure 4.9b) as a function of position along the radial distance at an arbitrary height (here we consider 1 mm) below the cavity. The plots are normalized with a factor of $\sqrt{H_r^2 + H_{z'}^2}$. We can see that the H_r is maximum at a distance ~7 mm from the symmetry axis of the cavity, right under the dielectric material.

One important factor to note is that ideally, the intra-cavity power should be Q-factor times the input MW power. However, in the present version of the cavity only 1% of the input power is going in to the cavity. In a future upgraded version, we plan to increase this coupling to at least 50%.

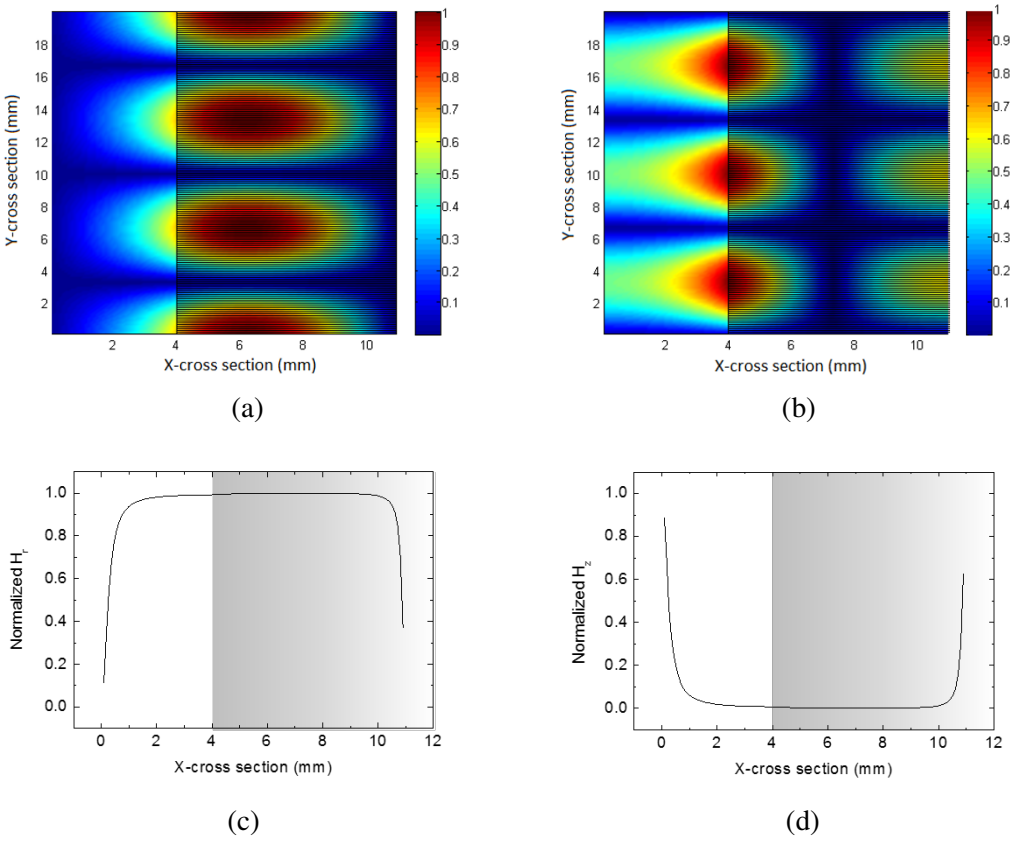

Figure 4.9: (**a**, **b**) Density plots for the normalized radial magnetic field ($H_r/\sqrt{H_r^2 + H_{z'}^2}$) and the normalized vertical magnetic field along the symmetry axis ($H_{z'}/\sqrt{H_r^2 + H_{z'}^2}$), respectively, as a function of the height above the bottom edge of the cavity (y-axis) and the distance from the symmetry axis of the cavity along the radius (x-axis). (**c**, **d**) Normalized radial magnetic field ($H_r/\sqrt{H_r^2 + H_{z'}^2}$) and normalized vertical magnetic field along the symmetry axis ($H_{z'}/\sqrt{H_r^2 + H_{z'}^2}$) as a function of the distance from the symmetry axis of the cavity along the radius at a 1 mm below the cavity. The shaded regions in all the four plots indicate the TiO_2 active dielectric medium [14].

5

Coupling nanodiamond NV centre to the MW field

The NV centre spin can be coupled to an external MW field. If the MW field is resonant with the ground state splitting, the spin can be coherently manipulation and its coherence properties can be characterized. This chapter discusses the results obtained from the experimental study of coupling a single NV centre to a resonant MW field. Two different methods are used to apply the MW field to the NV centre: a micro-wire and a MW cavity. Here we report and discuss observation of Rabi oscillations and the results of spin-echo measurements for both methods (section 5.2.2).

5.1 Identifying nanodiamonds with single NV centres

The first step in coupling single NV centres to the MW field is to locate a suitable nanodiamond. We prepare two different samples from the same batch of nanodiamonds, as

described in section 4.1, for both the micro-wire (section 4.5.1) and MW cavity methods (section 4.5.2). A micro-wire, working as a MW antenna is attached to one of the samples. Each sample is placed on the piezo stage of the confocal microscope for characterization (section 4.2). A 40×40 μm^2 area of the sample is scanned with the confocal microscope while the fluorescence is collected. The density plots for both samples, based on the fluorescence intensity are shown in figure 5.1. The nanodiamonds selected for the characterization are shown, marked by the white circles.

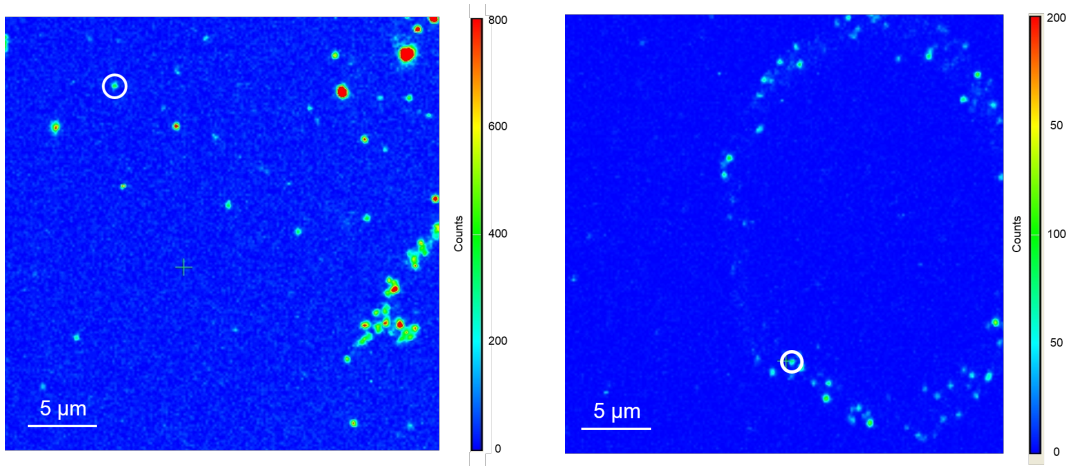

(a) (b)

Figure 5.1: (**a**) Confocal map of the 'micro-wire' sample. (**b**) Confocal map for the 'MW-cavity' sample. The NV centres characterized in depth in each sample are shown in the white circle.

We maximize the fluorescence intensity for each nanodiamond by adjusting the point of the focus in x, y and z. The photo-luminescence (PL) spectrum of the emitted nanodiamonds (figure 5.2) are recorded on the spectrometer (see section 4.2).

It is worth noting that the two spectra look rather different. While we know that both spectra belong to single NV centres (confirmed by autocorrelation and ODMR measurements, see below) the second one displays a much sharper phononic structure. We speculate that this might be related to the reduced size of the nanodiamond host affecting the phonon modes supported by the nanodiamond.

The correlation measurement for the nanodiamonds from both samples is performed by detecting the light emitted by the NVs via the HBT interferometer. In both cases, the centres

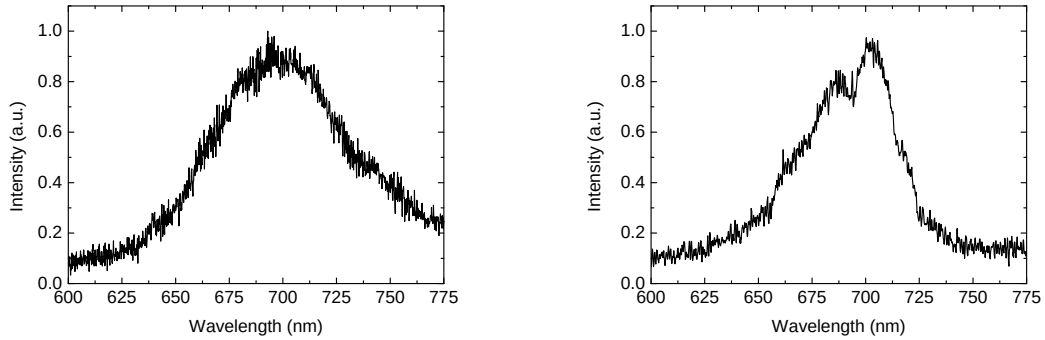

(a) (b)

Figure 5.2: (**a**) PL spectrum of the nanodiamond in the 'micro-wire' sample. (**b**) PL spectrum of the nanodiamond in the 'MW cavity' sample. The ZPL for the NV centres is at 637 nm, but hardly visible for the two samples.

are single NV emitters as shown by the antibunching dip of the autocorrelation function $g^{(2)}(\tau)$ as a function of τ (figure 5.3). In both cases, the anti-bunching is greater than ~80%, which indicates single NV centres (see section 4.3). The fact that $g^{(2)}(0)$ does not go down to zero completely, we attribute to background light.

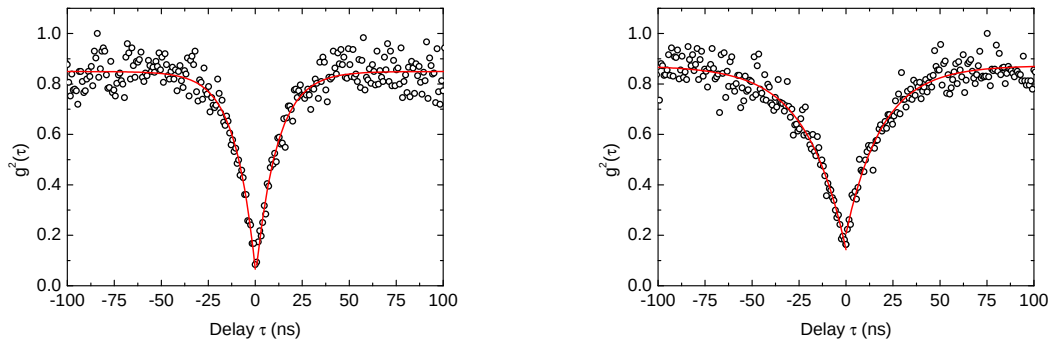

(a) (b)

Figure 5.3: Experimentally obtained auto-correlation function, $g^{(2)}(\tau)$ as a function of delay time τ for the target nanodiamonds in the micro-wire (**a**) and MW-cavity (**b**) samples.

5.2 Manipulating single NV centres with a MW field

Next, we perform the continuous-wave ODMR and pulsed ODMR measurements via coupling the MW field to the single NV centres.

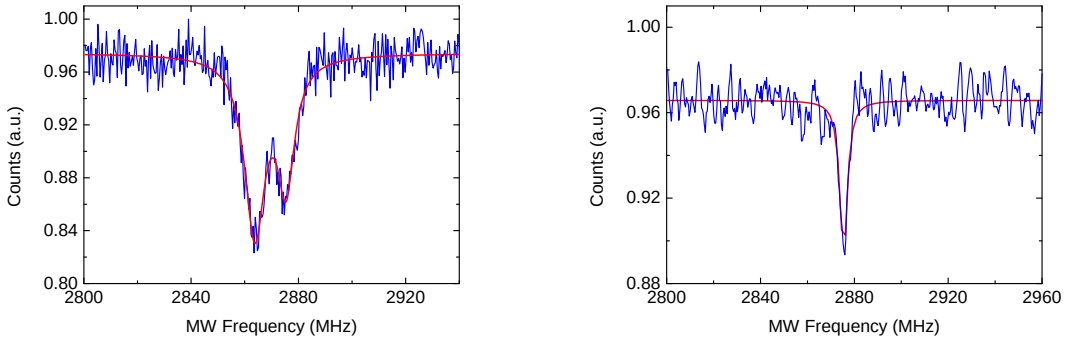

(a) (b)

Figure 5.4: Continuous wave ODMR measurement for single NV centres. (**a**) With the micro-wire sample. Two resonant frequencies are ~2.865 GHz and ~2.875 GHz and the contrast of the dip corresponding to ~2.865 GHz is ~13%. (**b**) With the MW cavity sample. The resonant frequency is ~2.875 GHz and the contrast is ~8%. Experimental data are in 'blue' while Lorentzian fit are in 'red'.

5.2.1 Continuous-wave ODMR measurement

A continuous MW signal generated by the MW signal generator and amplified by the MW amplifier is applied to the identified nanodiamonds with single NV centres, both for the micro-wire and MW-cavity sample. Sweeping the MW frequency, we perform continuous wave ODMR measurements for both cases (see section 4.4.1). For the micro-wire it is straightforward to obtain the ODMR spectrum with the maximum contrast (as shown in figure 5.4a). However, for the MW cavity case, maximizing the contrast requires two steps. First, an initial resonant frequency is found by sweeping the signal. Then, the ODMR contrast is maximized by mechanically moving the cavity position, as well as by tuning the resonance frequency (figure 5.5) of the cavity mode $TE_{0,1,3}$ to the resonant initial frequency found for the centre. This is done by means of the cavity plunger (see section 4.5.2). The ODMR spectrum of the MW cavity nanodiamond sample and the corresponding cavity spectrum are given in figures 5.4b and 5.5, respectively.

The result of the continuous wave ODMR measurement of the micro-wire sample is shown in figure 5.4a. The signal displays two resonant frequencies at ~2.865 GHz and ~2.875 GHz. This is due to the splitting of $m_s = +1$ and $m_s = -1$ due to the strain in the nanodiamond crystal. We choose the resonant frequency ~2.865 GHz with an ODMR contrast of ~13% for the pulsed ODMR studies with this sample. On the other hand, for the MW cavity sample we have only one resonant frequency with a contrast of ~8% (figure 5.4b). It has been reported

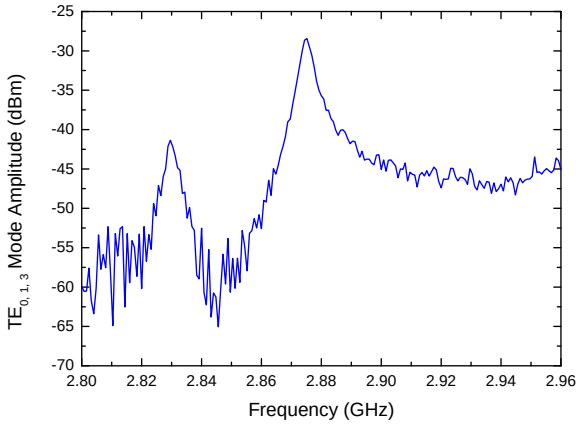

Figure 5.5: Cavity spectrum tuned to the NV centre ground state zero field splitting ~2.875 GHz.

[55] that only about ~15% of NV centres show no $m_s = +1/-1$ splitting resolvable via ODMR. It should also be noted that in the core of the MW-cavity the signal obtained is a convolution between the actual ODMR-NV spectrum and the transmission (figure 5.5) of the MW cavity acting like a filter.

5.2.2 Pulsed ODMR measurement

We perform Rabi oscillation and spin echo studies with pulsed ODMR measurements using both the micro-wire and MW cavity as the mode of applying MW. For this, we set the MW frequency for the micro-wire sample at ~2.865 GHz and for the MW cavity sample at ~2.875 GHz.

Rabi oscillation experiment

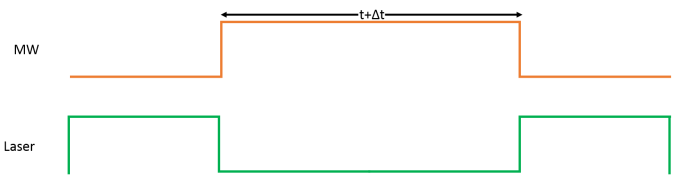

Figure 5.6: Pulse sequence of both the laser and MW for the Rabi oscillation measurements. The MW duration time (t) is increased by Δt at each step.

We apply the time-pulsed sequences for both laser and MW to the single NV centres (fig 5.6). The MW field is applied while the laser is 'off'. At each step we increase the MW pulse duration time by Δt. The NV fluorescence, after the second laser pulse, is recorded. The measurement is repeated and the output integrated over time. The Rabi oscillation for both the micro-wire sample and the MW cavity sample are shown in figures 5.7a and 5.7b, respectively. Experimental data points are shown, as well as a fit (continuous line) obtained with a 'sin-damp' function [32, 33]. The exponential decay superimposed to the Rabi nutation is related to the decoherence time T_2 (see section 2.4) of the NV centre.

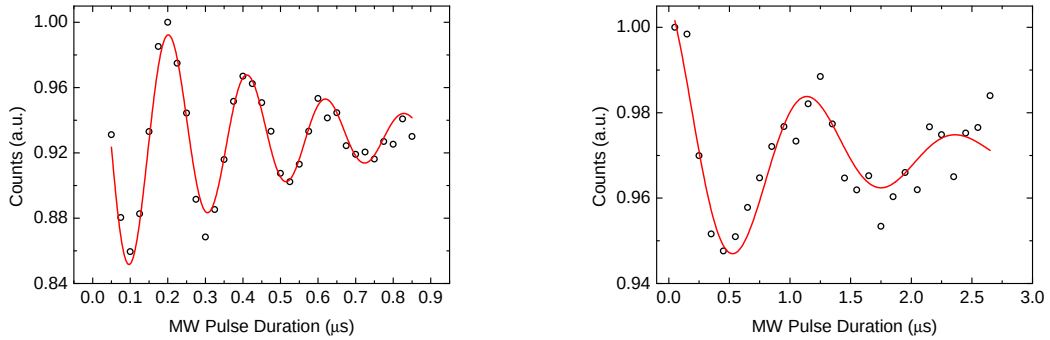

(a) (b)

Figure 5.7: Rabi oscillation for single NV centres. The circles are the experimental data points and the red curve is a 'sin-damp' function fitted to the experimental data points. (**a**) Micro-wire sample: The Rabi frequency is ~4.8 MHz and the π-pulse duration is ~104 ns. (**b**) MW cavity sample: The Rabi frequency is ~0.83 MHz and the π-pulse duration is ~612 ns.

Note, how the Rabi oscillation is slower in the case of the cavity (figure 5.7b). The Rabi frequency of the oscillation we obtained is ~0.82 MHz and the corresponding π-pulse duration is ~612 ns. This is somewhat expected as, unlike in the case of the micro-wire antenna, the cavity in its current design transmits only ~1% of the MW power [14], resulting in a slower nutation of the NV ground spin state.

To verify the variation in the Rabi oscillation frequency (Ω_r), we vary the MW power (P_{MW}) and plot the Ω_r as a function of P_{MW} (figure 2.6). The fit to the experimental points shows that the $\Omega_r \propto \sqrt{P_{MW}}$ as expected. The Rabi frequency scales as $\Omega_r \propto H$ (see section 2.3.2) and the MW power $P_{MW} \propto H^2$. Thus $\Omega_r \propto \sqrt{P_{MW}}$. Indeed, the fit to the experimental data points shows the expected proportionality of Ω_r to $\sqrt{P_{MW}}$.

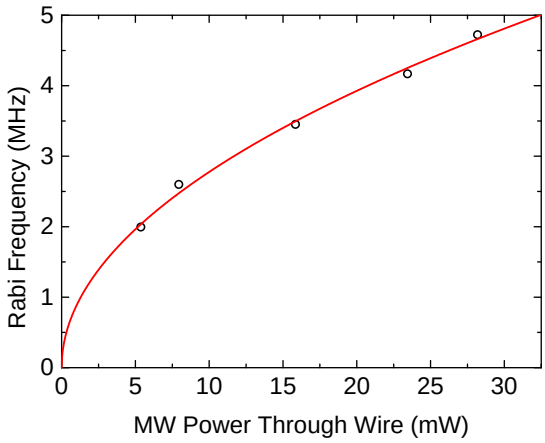

Figure 5.8: MW power dependence of Rabi frequency. The circles are the experimental data points and the red curve is the fit with a function $\propto \sqrt{P_{MW}}$.

Spin-echo studies

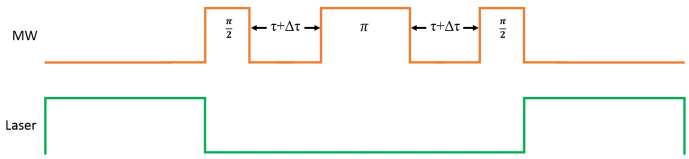

Figure 5.9: Pulse sequence of both the laser and MW for the spin-echo measurements. The delay time (τ) is increased by $\Delta\tau$ at each step.

With the π-pulse extracted from the Rabi oscillation experiments, we are now in a position to apply the appropriate pulse sequence for the spin-echo study (see section 4.4.2). In order to read the spin-echo signal as a function of time, the delay time τ is consecutively increased by $\Delta\tau$; from shot to shot the fluorescence from the NV centre is then recorded after each pulse sequence and integrated over time. The normalized photon counts are plotted as a function of twice the time delay τ (i.e. 2τ) [60]. The results are shown in figure 5.10. An exponential fit is applied to the experimental points, from which we get a value for the coherence time T_2 of ~3.7 μs (in the case of the wire).

The coherence time of a single NV centre of ~3.7 μs obtained with the micro-wire sample, is actually consistent with the one which we considered for the coupling to the flux qubits (section 3.3.3). Though we considered the ensemble case for the flux qubit analysis, the value we determined here is extremely promising as it is at room temperature. One can expect a

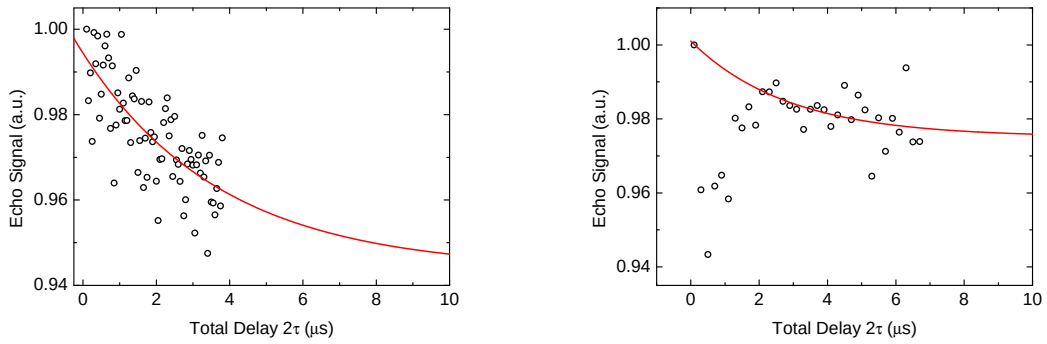

(a) (b)

Figure 5.10: Spin-echo measurements with single NV centres. The circles are the experimental data points and the red curve is an 'exponential decay' function fitted to the experimental data points. (**a**) With the micro-wire sample. The π-pulse duration is ~104 ns. The coherence time obtained is ~3.7μs. (**b**) With the MW cavity sample. The π-pulse duration is ~612 ns.

considerable increase in the coherence time at the working temperature of the flux qubits of a few tens of milli-Kelvin, since the centre would be almost completely decoupled from the surrounding spin bath.

It is worth noting that the measurement of T_2 performed with the cavity (figure 5.10b) shows an unexpected behaviour, with a pronounced dip in fluorescence for short delay time τ. This is somewhat baffling as one should expect high fluorescence intensities when τ is small and hence the NV had not yet had time to lose its coherence. We are conducting an in-depth analysis of this behaviour at the time this thesis is being submitted. Currently, we speculate that due to the high Q-factor the microwave cavity is altering the shape of the MW pulses, with this effect being particularly critical at shorter time scales (~hundreds of ns). In figure 5.10b, we nevertheless fit the experimental data with an exponential decay excluding the points for $\tau < 1$ μs. The fit gives an indicative value for T_2 of ~2.8 μs, which is–as expected–almost three times longer than the decay time of the Rabi nutation: $T_{2,Rabi} = 1.1$ μs [60]. However, given the initial unexplained fluorescence dip, this value has to be definitely taken with a grain of salt.

When theory and experiment agree, that is the time to be especially suspicious.

Niels Bohr

6

Conclusions and future outlooks

In the first part of this thesis, we have investigated and shown that the coherent coupling of ensembles of NV centres in a nanodiamond crystal to a gap-flux qubit is possible. The novelty of this result is that the coherent coupling is possible with considerably less spins than previously reported in the literature. We have calculated this by considering the precise positioning of the nanodiamonds on the flux qubit. The optimum requirement including the uncertainty related to the precise positioning of the nanodiamond with respect to the flux qubit have been calculated and discussed. It is shown that the tolerance is well within our experimental capabilities. Most importantly, we have studied the effect on the NV-flux qubit coupling due to the randomness of the NV's quantization axis resulting from the random orientation of the nanocrystal. The results show that irrespective of the orientation of the nanodiamond, we can coherently couple one of the subensembles of NVs out of the four geometrically possible, given the tetrahedral symmetry of the diamond lattice.

In the second part of this thesis, we experimentally studied the spin manipulation and spin-echo measurements of a single NV centre with a MW field both using a micro-wire antenna and a custom-designed MW cavity. With the micro-wire we observed the Rabi oscillation of the NV's $m_s = 0 \leftrightarrow m_s = \pm 1$ ground state and estimated an experimental value for the coherence time of ~3.7 μs for a single NV centre in the diamond nanocrystal. This value is reasonable for the coupling to the flux qubit as we estimated numerically for reaching efficient coupling. We also tested the suitability of the MW cavity-which was designed newly in our group-for NV spin manipulation experiments. We observed the Rabi oscillation with the MW cavity for a single NV centre in a sample from the same nanodiamond batch we used for the characterization with the micro-wire. Our results also showed, however, that further work needs to be done to optimize the transmitted power of the MW-cavity to produce reliable spin-echo measurements.

In the future, we plan to experimentally study the coupling of NV centres in nanodiamonds with flux qubits in collaboration with researchers within the Australian Research Council Centre of Excellence for Engineered Quantum Systems (EQUS). As a step forward to this, we plan to study the coherence time for an ensemble of NV centres. We also project to conduct a study to characterize the coherence time of NV centres in relation to surface effects, since this can help us better understand and ultimately control their coherence time. Specifically, we plan on using the flexibility of the MW cavity to study how the size of the nanodiamond host affects the coherence time of the NV centre. To do this we will carry out consecutive air oxidation steps on individual nanocrystals and after each oxidation step re-measure the coherence properties of the NV spins. The open cavity design with the large-scale delivery of MW power will facilitate their study [61]. As step we will redesign the MW cavity to achieve near-cavity coupling efficiencies of the MW signals to the cavity. In addition to the systematic size studies we plan to pursue low-temperature magnetic field sensing experiments with our nanodiamond NV centres.

A

Appendix

A.1 Magnetic field generated by the gap tunable flux qubit

The magnetic field components B_x, B_y and B_z generated by the gap-tunable flux qubit at an arbitrary point $((\beta - \frac{l}{2}), \gamma, (b - \frac{q}{2} - \alpha))$ (represented by red dot in figure (A.1)), calculated using the Biot-Savart law are given in equations A.1, A.2, A.3. The origin of the co-ordinate system is assumed to be at the centre of the superconducting bridge (represented by 'o' in figure A.1).

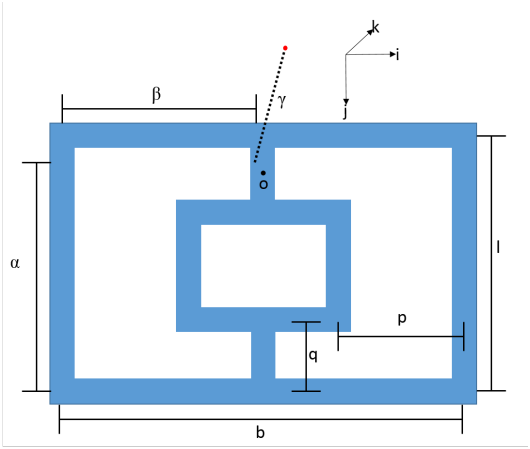

Figure A.1: Top view of the flux qubit. Parameters to calculate the magnetic field components generated by the gap tunable flux qubit at an arbitrary point $((\beta-\frac{l}{2}), \gamma, (b-\frac{q}{2}-\alpha))$ (represented in red dot) is given. The origin is assumed to be at the centre of the bridge (represented by 'o').

$$B_x = \frac{\mu_0}{4\pi} i\gamma \left(\frac{2\left(\frac{l-\alpha}{\sqrt{(l-\alpha)^2+\left(\frac{b}{2}-\beta\right)^2+\gamma^2}} + \frac{\alpha}{\sqrt{\alpha^2+\left(\frac{b}{2}-\beta\right)^2+\gamma^2}} + \frac{q-\alpha}{\sqrt{(-q+\alpha)^2+\left(\frac{b}{2}-\beta\right)^2+\gamma^2}} + \frac{-l+q+\alpha}{\sqrt{(-l+q+\alpha)^2+\left(\frac{b}{2}-\beta\right)^2+\gamma^2}} \right)}{\left(\frac{b}{2}-\beta\right)^2+\gamma^2} \right.$$

$$- \frac{\frac{l-\alpha}{\sqrt{(l-\alpha)^2+(b-\beta)^2+\gamma^2}} + \frac{\alpha}{\sqrt{\alpha^2+(b-\beta)^2+\gamma^2}}}{(b-\beta)^2+\gamma^2} + \frac{\frac{-q+\alpha}{\sqrt{(-q+\alpha)^2+(b-p-\beta)^2+\gamma^2}} + \frac{l-q-\alpha}{\sqrt{(-l+q+\alpha)^2+(b-p-\beta)^2+\gamma^2}}}{(b-p-\beta)^2+\gamma^2}$$

$$\left. - \frac{\frac{l-\alpha}{\sqrt{(l-\alpha)^2+\beta^2+\gamma^2}} + \frac{\alpha}{\sqrt{\alpha^2+\beta^2+\gamma^2}}}{\beta^2+\gamma^2} + \frac{\frac{-q+\alpha}{\sqrt{(-q+\alpha)^2+(-p+\beta)^2+\gamma^2}} + \frac{l-q-\alpha}{\sqrt{(-l+q+\alpha)^2+(-p+\beta)^2+\gamma^2}}}{(-p+\beta)^2+\gamma^2} \right) \quad (A.1)$$

$$
\begin{aligned}
B_y = \frac{\mu_0}{4\pi} i \Bigg(& \frac{2\left(\frac{b}{2}-\beta\right)\left(\frac{l-\alpha}{\sqrt{(l-\alpha)^2+\left(\frac{b}{2}-\beta\right)^2+\gamma^2}}+\frac{\alpha}{\sqrt{\alpha^2+\left(\frac{b}{2}-\beta\right)^2+\gamma^2}}+\frac{q-\alpha}{\sqrt{(-q+\alpha)^2+\left(\frac{b}{2}-\beta\right)^2+\gamma^2}}+\frac{-l+q+\alpha}{\sqrt{(-l+q+\alpha)^2+\left(\frac{b}{2}-\beta\right)^2+\gamma^2}}\right)}{\left(\frac{b}{2}-\beta\right)^2+\gamma^2} \\
& - \frac{(b-\beta)\left(\frac{l-\alpha}{\sqrt{(l-\alpha)^2+(b-\beta)^2+\gamma^2}}+\frac{\alpha}{\sqrt{\alpha^2+(b-\beta)^2+\gamma^2}}\right)}{(b-\beta)^2+\gamma^2} + \frac{(b-p-\beta)\left(\frac{-q+\alpha}{\sqrt{(-q+\alpha)^2+(b-p-\beta)^2+\gamma^2}}+\frac{l-q-\alpha}{\sqrt{(-l+q+\alpha)^2+(b-p-\beta)^2+\gamma^2}}\right)}{(b-p-\beta)^2+\gamma^2} \\
& + \frac{(l-\alpha)\left(\frac{b-2\beta}{\sqrt{(l-\alpha)^2+\left(\frac{b}{2}-\beta\right)^2+\gamma^2}}-\frac{b-\beta}{\sqrt{(l-\alpha)^2+(b-\beta)^2+\gamma^2}}+\frac{\beta}{\sqrt{(l-\alpha)^2+\beta^2+\gamma^2}}\right)}{(l-\alpha)^2+\gamma^2} + \frac{\beta\left(\frac{l-\alpha}{\sqrt{(l-\alpha)^2+\beta^2+\gamma^2}}+\frac{\alpha}{\sqrt{\alpha^2+\beta^2+\gamma^2}}\right)}{\beta^2+\gamma^2} \\
& + \frac{\alpha\left(\frac{b-2\beta}{\sqrt{\alpha^2+\left(\frac{b}{2}-\beta\right)^2+\gamma^2}}-\frac{b-\beta}{\sqrt{\alpha^2+(b-\beta)^2+\gamma^2}}+\frac{\beta}{\sqrt{\alpha^2+\beta^2+\gamma^2}}\right)}{\alpha^2+\gamma^2} + \frac{(-q+\alpha)\left(\frac{-b+2\beta}{\sqrt{(-q+\alpha)^2+\left(\frac{b}{2}-\beta\right)^2+\gamma^2}}+\frac{b-p-\beta}{\sqrt{(-q+\alpha)^2+(b-p-\beta)^2+\gamma^2}}-\frac{-p+\beta}{\sqrt{(-q+\alpha)^2+(-p+\beta)^2+\gamma^2}}\right)}{(-q+\alpha)^2+\gamma^2} \\
& - \frac{(-p+\beta)\left(\frac{-q+\alpha}{\sqrt{(-q+\alpha)^2+(-p+\beta)^2+\gamma^2}}+\frac{l-q-\alpha}{\sqrt{(-l+q+\alpha)^2+(-p+\beta)^2+\gamma^2}}\right)}{(-p+\beta)^2+\gamma^2} + \frac{(-l+q+\alpha)\left(\frac{b-2\beta}{\sqrt{(-l+q+\alpha)^2+\left(\frac{b}{2}-\beta\right)^2+\gamma^2}}-\frac{b-p-\beta}{\sqrt{(-l+q+\alpha)^2+(b-p-\beta)^2+\gamma^2}}+\frac{-p+\beta}{\sqrt{(-l+q+\alpha)^2+(-p+\beta)^2+\gamma^2}}\right)}{(-l+q+\alpha)^2+\gamma^2} \Bigg)
\end{aligned}
\tag{A.2}
$$

$$
\begin{aligned}
|B_z = \frac{\mu_0}{4\pi} i\gamma \Bigg(& \frac{\frac{-b+2\beta}{\sqrt{(l-\alpha)^2+\left(\frac{b}{2}-\beta\right)^2+\gamma^2}}+\frac{b-\beta}{\sqrt{(l-\alpha)^2+(b-\beta)^2+\gamma^2}}-\frac{\beta}{\sqrt{(l-\alpha)^2+\beta^2+\gamma^2}}}{(l-\alpha)^2+\gamma^2} + \frac{\frac{b-2\beta}{\sqrt{\alpha^2+\left(\frac{b}{2}-\beta\right)^2+\gamma^2}}-\frac{b-\beta}{\sqrt{\alpha^2+(b-\beta)^2+\gamma^2}}+\frac{\beta}{\sqrt{\alpha^2+\beta^2+\gamma^2}}}{\alpha^2+\gamma^2} \\
& + \frac{\frac{-b+2\beta}{\sqrt{(-q+\alpha)^2+\left(\frac{b}{2}-\beta\right)^2+\gamma^2}}+\frac{b-p-\beta}{\sqrt{(-q+\alpha)^2+(b-p-\beta)^2+\gamma^2}}-\frac{-p+\beta}{\sqrt{(-q+\alpha)^2+(-p+\beta)^2+\gamma^2}}}{(-q+\alpha)^2+\gamma^2} \\
& + \frac{\frac{b-2\beta}{\sqrt{(-l+q+\alpha)^2+\left(\frac{b}{2}-\beta\right)^2+\gamma^2}}-\frac{b-p-\beta}{\sqrt{(-l+q+\alpha)^2+(b-p-\beta)^2+\gamma^2}}+\frac{-p+\beta}{\sqrt{(-l+q+\alpha)^2+(-p+\beta)^2+\gamma^2}}}{(-l+q+\alpha)^2+\gamma^2} \Bigg)
\end{aligned}
\tag{A.3}
$$

List of Symbols

The following list is neither exhaustive nor exclusive, but may be helpful.

$\hbar$ ..... reduced Planck's constant

S_x, S_y, S_z .... spin-1 matrices

σ_x, σ_y, σ_z .. Pauli spin-1/2 matrices

D_g ..... ground state zero field splitting

E ..... strain induced splitting

T_2 ..... coherence time

G ..... collective coupling strength

$g^{(2)}(\tau)$ ..... second order correlation function

References

[1] C. Bradac. *The properties of nitrogen-vacancy centres in nanodiamond*. Thesis, Macquarie University, North Ryde, N.S.W. (2012).

[2] C. Wang. *A solid-state single photon source based on color centers in diamond*. Ph.D. thesis, lmu (2007).

[3] D. Zheng. *Study and manipulation of photoluminescent NV color center in diamond*. Ph.D. thesis, École normale supérieure de Cachan-ENS Cachan; East China Normal University (2010).

[4] A. M. Zaitsev. *Optical properties of diamond: a data handbook* (Springer Science & Business Media, 2013).

[5] J. Wrachtrup. *Defect center room-temperature quantum processors*. PNAS **107**(21), 9479 (2010).

[6] G. Balasubramanian, P. Neumann, D. Twitchen, M. Markham, R. Kolesov, N. Mizuochi, J. Isoya, J. Achard, J. Beck, J. Tissler, *et al. Ultralong spin coherence time in isotopically engineered diamond*. Nature materials **8**(5), 383 (2009).

[7] D. Marcos, M. Wubs, J. Taylor, R. Aguado, M. Lukin, and A. S. Sørensen. *Coupling nitrogen-vacancy centers in diamond to superconducting flux qubits*. Physical review letters **105**(21), 210501 (2010).

[8] Z.-L. Xiang, S. Ashhab, J. You, and F. Nori. *Hybrid quantum circuits: Superconducting circuits interacting with other quantum systems*. Reviews of Modern Physics **85**(2), 623 (2013).

[9] J. Twamley and S. Barrett. *Superconducting cavity bus for single nitrogen-vacancy defect centers in diamond*. Physical Review B **81**(24), 241202 (2010).

[10] X. Zhu, S. Saito, A. Kemp, K. Kakuyanagi, S.-i. Karimoto, H. Nakano, W. J. Munro, Y. Tokura, M. S. Everitt, K. Nemoto, *et al. Coherent coupling of a superconducting flux qubit to an electron spin ensemble in diamond*. Nature **478**(7368), 221 (2011).

[11] S. Saito, X. Zhu, R. Amsüss, Y. Matsuzaki, K. Kakuyanagi, T. Shimo-Oka, N. Mizuochi, K. Nemoto, W. J. Munro, and K. Semba. *Towards realizing a quantum memory for a superconducting qubit: Storage and retrieval of quantum states*. Physical review letters **111**(10), 107008 (2013).

[12] X. Zhu, Y. Matsuzaki, R. Amsüss, K. Kakuyanagi, T. Shimo-Oka, N. Mizuochi, K. Nemoto, K. Semba, W. J. Munro, and S. Saito. *Observation of dark states in a superconductor diamond quantum hybrid system*. Nature communications **5** (2014).

[13] Y. Matsuzaki, X. Zhu, K. Kakuyanagi, H. Toida, T. Shimooka, N. Mizuochi, K. Nemoto, K. Semba, W. Munro, H. Yamaguchi, *et al. Improving the lifetime of the nitrogen-vacancy-center ensemble coupled with a superconducting flux qubit by applying magnetic fields*. Physical Review A **91**(4), 042329 (2015).

[14] J.-M. Le Floch, C. Bradac, N. Nand, S. Castelletto, M. Tobar, and T. Volz. *Addressing a single spin in diamond with a macroscopic dielectric microwave cavity*. Applied Physics Letters **105**(13), 133101 (2014).

[15] M. W. Doherty, N. B. Manson, P. Delaney, F. Jelezko, J. Wrachtrup, and L. C. Hollenberg. *The nitrogen-vacancy colour centre in diamond*. Physics Reports **528**(1), 1 (2013).

[16] J. Loubser and J. van Wyk. *Electron spin resonance in the study of diamond*. Reports on Progress in Physics **41**(8), 1201 (1978).

[17] G. Davies. *Dynamic jahn-teller distortions at trigonal optical centres in diamond*. Journal of Physics C: Solid State Physics **12**(13), 2551 (1979). URL http://stacks.iop.org/0022-3719/12/i=13/a=019.

[18] L. Du Preez. *Electron paramagnetic resonance and optical investigations of defect centres in diamond*. Ph.D. thesis, University of The Witwatersrand, 1965. Typescript. (1965).

[19] L. Rondin, J. Tetienne, T. Hingant, J. Roch, P. Maletinsky, and V. Jacques. *Magnetometry with nitrogen-vacancy defects in diamond*. Reports on Progress in Physics **77**(5), 056503 (2014).

[20] E. O. Schäfer-Nolte. *Development of a diamond-based scanning probe spin sensor operating at low temperature in ultra high vacuum* (2014).

[21] M. W. Doherty, N. B. Manson, P. Delaney, and L. C. Hollenberg. *The negatively charged nitrogen-vacancy centre in diamond: the electronic solution*. New Journal of Physics **13**(2), 025019 (2011).

[22] V. M. Acosta. *Optical magnetometry with nitrogen-vacancy centers in diamond* (2011).

[23] L. Rogers, S. Armstrong, M. Sellars, and N. Manson. *Infrared emission of the nv centre in diamond: Zeeman and uniaxial stress studies*. New Journal of Physics **10**(10), 103024 (2008).

[24] V. Acosta, A. Jarmola, E. Bauch, and D. Budker. *Optical properties of the nitrogen-vacancy singlet levels in diamond*. Physical Review B **82**(20), 201202 (2010).

[25] J. Loubser and J. Van Wyk. *Optical spin-polarisation in a triplet state in irradiated and annealed type 1b diamonds* (1977).

[26] N. Reddy, N. Manson, and E. Krausz. *Two-laser spectral hole burning in a colour centre in diamond*. Journal of Luminescence **38**(1), 46 (1987).

[27] G. Fuchs, V. Dobrovitski, R. Hanson, A. Batra, C. Weis, T. Schenkel, and D. Awschalom. *Excited-state spectroscopy using single spin manipulation in diamond*. Physical review letters **101**(11), 117601 (2008).

[28] P. Neumann, R. Kolesov, V. Jacques, J. Beck, J. Tisler, A. Batalov, L. Rogers, N. Manson, G. Balasubramanian, F. Jelezko, *et al. Excited-state spectroscopy of single nv defects in diamond using optically detected magnetic resonance*. New Journal of Physics **11**(1), 013017 (2009).

[29] A. Batalov, C. Zierl, T. Gaebel, P. Neumann, I.-Y. Chan, G. Balasubramanian, P. Hemmer, F. Jelezko, and J. Wrachtrup. *Temporal coherence of photons emitted by single nitrogen-vacancy defect centers in diamond using optical rabi-oscillations*. Physical review letters **100**(7), 077401 (2008).

[30] Y. Chu, M. Markham, D. J. Twitchen, and M. D. Lukin. *All-optical control of a single electron spin in diamond*. Physical Review A **91**(2), 021801 (2015).

[31] P. Neumann. *Towards a room temperature solid state quantum processor-the nitrogen-vacancy center in diamond* (2012).

[32] F. Jelezko and J. Wrachtrup. *Read-out of single spins by optical spectroscopy*. Journal of Physics: Condensed Matter **16**(30), R1089 (2004).

[33] F. Jelezko, T. Gaebel, I. Popa, A. Gruber, and J. Wrachtrup. *Observation of coherent oscillations in a single electron spin*. Physical review letters **92**(7), 076401 (2004).

[34] A. Jarmola, V. Acosta, K. Jensen, S. Chemerisov, and D. Budker. *Temperature-and magnetic-field-dependent longitudinal spin relaxation in nitrogen-vacancy ensembles in diamond*. Physical review letters **108**(19), 197601 (2012).

[35] F. Jelezko and J. Wrachtrup. *Single defect centres in diamond: A review*. physica status solidi (a) **203**(13), 3207 (2006).

[36] L. M. Pham. *Magnetic field sensing with nitrogen-vacancy color centers in diamond*. Tech. rep., DTIC Document (2013).

[37] C. H. Van der Wal, A. Ter Haar, F. Wilhelm, R. Schouten, C. Harmans, T. Orlando, S. Lloyd, and J. Mooij. *Quantum superposition of macroscopic persistent-current states*. Science **290**(5492), 773 (2000).

[38] J. Mooij, T. Orlando, L. Levitov, L. Tian, C. H. Van der Wal, and S. Lloyd. *Josephson persistent-current qubit*. Science **285**(5430), 1036 (1999).

[39] F. G. Paauw. *Superconducting flux qubits: Quantum chains and tunable qubits* (TU Delft, Delft University of Technology, 2009).

[40] M. Schwarz, J. Goetz, Z. Jiang, T. Niemczyk, F. Deppe, A. Marx, and R. Gross. *Gradiometric flux qubits with a tunable gap*. New Journal of Physics **15**(4), 045001 (2013).

[41] A. Fedorov, A. Feofanov, P. Macha, P. Forn-Díaz, C. Harmans, and J. Mooij. *Strong coupling of a quantum oscillator to a flux qubit at its symmetry point*. Physical review letters **105**(6), 060503 (2010).

[42] A. Fedorov, P. Macha, A. Feofanov, C. Harmans, and J. Mooij. *Tuned transition from quantum to classical for macroscopic quantum states*. Physical review letters **106**(17), 170404 (2011).

[43] F. Yoshihara, K. Harrabi, A. Niskanen, Y. Nakamura, and J. Tsai. *Decoherence of flux qubits due to 1/f flux noise*. Physical review letters **97**(16), 167001 (2006).

[44] K. Kakuyanagi, T. Meno, S. Saito, H. Nakano, K. Semba, H. Takayanagi, F. Deppe, and A. Shnirman. *Dephasing of a superconducting flux qubit*. Physical review letters **98**(4), 047004 (2007).

[45] X. Zhu, A. Kemp, S. Saito, and K. Semba. *Coherent operation of a gap-tunable flux qubit*. Applied Physics Letters **97**(10), 102503 (2010).

[46] F. Paauw, A. Fedorov, C. M. Harmans, and J. Mooij. *Tuning the gap of a superconducting flux qubit*. Physical review letters **102**(9), 090501 (2009).

[47] Y. Matsuzaki, X. Zhu, K. Kakuyanagi, H. Toida, T. Shimo-Oka, N. Mizuochi, K. Nemoto, K. Semba, W. J. Munro, H. Yamaguchi, *et al. Improving the coherence time of a quantum system via a coupling to a short-lived system*. Physical review letters **114**(12), 120501 (2015).

[48] C. Bradac, T. Gaebel, C. Pakes, J. M. Say, A. V. Zvyagin, J. R. Rabeau, *et al. Effect of the nanodiamond host on a nitrogen-vacancy color-centre emission state*. Small **9**(1), 132 (2013).

[49] C.-C. Fu, H.-Y. Lee, K. Chen, T.-S. Lim, H.-Y. Wu, P.-K. Lin, P.-K. Wei, P.-H. Tsao, H.-C. Chang, and W. Fann. *Characterization and application of single fluorescent nanodiamonds as cellular biomarkers*. Proceedings of the National Academy of Sciences **104**(3), 727 (2007).

[50] M. Stern, G. Catelani, Y. Kubo, C. Grezes, A. Bienfait, D. Vion, D. Esteve, and P. Bertet. *Flux qubits with long coherence times for hybrid quantum circuits*. Physical review letters **113**(12), 123601 (2014).

[51] P. Bertet, I. Chiorescu, G. Burkard, K. Semba, C. Harmans, D. P. DiVincenzo, and J. Mooij. *Dephasing of a superconducting qubit induced by photon noise*. Physical review letters **95**(25), 257002 (2005).

[52] S. Takahashi, R. Hanson, J. van Tol, M. S. Sherwin, and D. D. Awschalom. *Quenching spin decoherence in diamond through spin bath polarization*. Physical review letters **101**(4), 047601 (2008).

[53] Y. Kubo, F. Ong, P. Bertet, D. Vion, V. Jacques, D. Zheng, A. Dréau, J.-F. Roch, A. Auffèves, F. Jelezko, *et al. Strong coupling of a spin ensemble to a superconducting resonator*. Physical Review Letters **105**(14), 140502 (2010).

[54] I. Diniz, S. Portolan, R. Ferreira, J. Gérard, P. Bertet, and A. Auffeves. *Strongly coupling a cavity to inhomogeneous ensembles of emitters: Potential for long-lived solid-state quantum memories*. Physical Review A **84**(6), 063810 (2011).

[55] A. Gruber, A. Dräbenstedt, C. Tietz, L. Fleury, J. Wrachtrup, and C. Von Borczyskowski. *Scanning confocal optical microscopy and magnetic resonance on single defect centers*. Science **276**(5321), 2012 (1997).

[56] C. Kurtsiefer, S. Mayer, P. Zarda, and H. Weinfurter. *Stable solid-state source of single photons*. Physical review letters **85**(2), 290 (2000).

[57] A. Beveratos, R. Brouri, T. Gacoin, J.-P. Poizat, and P. Grangier. *Nonclassical radiation from diamond nanocrystals*. Physical Review A **64**(6), 061802 (2001).

[58] E. Donley, T. Heavner, F. Levi, M. Tataw, and S. Jefferts. *Double-pass acousto-optic modulator system*. Review of Scientific Instruments **76**(6), 063112 (2005).

[59] J.-M. Le Floch, Y. Fan, G. Humbert, Q. Shan, D. Férachou, R. Bara-Maillet, M. Aubourg, J. G. Hartnett, V. Madrangeas, D. Cros, *et al. Invited article: Dielectric material characterization techniques and designs of high-q resonators for applications from micro to millimeter-waves frequencies applicable at room and cryogenic temperatures*. Review of Scientific Instruments **85**(3), 031301 (2014).

[60] R. Hanson, O. Gywat, and D. Awschalom. *Room-temperature manipulation and decoherence of a single spin in diamond*. Physical Review B **74**(16), 161203 (2006).

[61] T. Gaebel, C. Bradac, J. Chen, J. Say, L. Brown, P. Hemmer, and J. Rabeau. *Size-reduction of nanodiamonds via air oxidation*. Diamond and Related Materials **21**, 28 (2012).